The role of intraspinal sensory neurons in the control of quadrupedal locomotion

Gerstmann K., Jurčić N., Blasco E., Kunz S., de Almeida Sassi F., Wanaverbecq N., Zampieri N.

This is the final version of the accepted manuscript. The original article has been published in final edited form in:

Current Biology
2022 JUN 06 ; 32(11): 2442-2453
2022 MAY 04 (first published online: final publication)
doi: 10.1016/j.cub.2022.04.019

Publisher: Cell Press / Elsevier

The role of intraspinal sensory neurons in the control of quadrupedal locomotion

Katrin Gerstmann[1], Nina Jurčić[2], Edith Blasco[2], Severine Kunz[3], Felipe de Almeida Sassi[1], Nicolas Wanaverbecq[2] and Niccolò Zampieri[1*]

[1]Max-Delbrück-Center for Molecular Medicine,
Robert-Rössle-Str. 10, 13125 Berlin, Germany.

[2]Aix-Marseille Université & CNRS, UMR 7289, Institut de Neurosciences de la Timone, SpiCCI Team, Timone Campus, 27 Boulevard Jean Moulin, 13005, Marseille, France.

[3]Technology Platform for Electron Microscopy, Max-Delbrück-Center for Molecular Medicine,
Robert-Rössle-Str. 10, 13125 Berlin, Germany.

*Lead Contact

Correspondence : niccolo.zampieri@mdc-berlin.de

Twitter: @ZampieriNiccolo

Summary

From swimming to walking and flying, animals have evolved specific locomotor strategies to thrive in different habitats. All types of locomotion depend on integration of motor commands and sensory information to generate precisely coordinated movements. Cerebrospinal fluid-contacting neurons (CSF-cN) constitute a vertebrate sensory system that monitors CSF composition and flow. In fish, CSF-cN modulate swimming activity in response to changes in pH and bending of the spinal cord, yet their role in mammals remains unknown. We used mouse genetics to study their function in quadrupedal locomotion. We found that CSF-cN are directly integrated into spinal motor circuits. Perturbation of CSF-cN function does not affect general motor activity nor the generation of locomotor rhythm and pattern, but results in specific defects in skilled movements. These results identify a role for mouse CSF-cN in adaptive motor control and indicate that this sensory system evolved a novel function to accommodate the biomechanical requirements of limb-based locomotion.

Introduction

Animals have developed a wide variety of locomotor strategies to adapt to their environment. The ability to precisely control movements is essential for each mode of locomotion and depends on the dynamic integration of motor commands and sensory information. Planning and initiation of motor programs take place in the brain, while their execution is directed by the spinal cord. Spinal circuits combine descending input with sensory feedback in order to generate coordinated movements and reflexive actions[1–3]. While the contributions of the somatosensory system have been extensively studied, the role of different sources of sensory information is less clear.

CSF-cN have been first described a century ago as sensory neurons lining the central canal in vertebrates[4,5]. They exhibit a peculiar morphology including a ciliated protrusion extending into the lumen of the central canal[6]. Thus, they have been thought to represent a sensory system monitoring CSF composition and flow. CSF-cN are inhibitory neurons and express ion channels known to be involved in sensory transduction, such as P2X and Pkd2l1[7,8]. The latter represents a specific marker of CSF-cN[9]. In larval zebrafish, CSF-cN are directly connected to primary motor neurons and V0v interneurons, glutamatergic premotor neurons that are part of the swimming central pattern generator[10,11]. Optogenetic stimulation of CSF-cN in resting larvae elicits low frequency movements, while activation during active swimming results in inhibition of locomotion, thus indicating that CSF-cN differentially modulate motor activity depending on the state of the animal[10].

In fish, CSF-cN sense changes in pH and spinal curvature[12–14]. In particular, calcium imaging experiments revealed responses to both active and passive bending of the body axis, highlighting CSF-cN function as a mechanosensory system detecting the curvature of the spinal cord, either self-generated or induced by external forces[11,12]. Pkd2l1 has been shown to be crucial for CSF-cN mechanosensory function, in its absence CSF-cN are not activated by spinal

bending and behavioral responses are impaired[12,15]. Altogether these studies indicate that in fish CSF-cN are the key component of a chemo- and mechanoreceptive sensory system that relay information about CSF composition and curvature of the body axis in order to modulate locomotor activity and control posture[16].

The biomechanical requirements and circuit mechanisms controlling wave-like propagation of swimming movements in fish versus on-ground locomotion in limbed vertebrates are substantially different, raising questions regarding the physiological function of CSF-cN[17]. In this study, we analyzed CSF-cN connectivity and function in mice. We found that CSF-cN are directly integrated in spinal motor circuits and form ascending recurrent connections. Ablation of CSF-cN did not affect motor activity nor the generation of stereotyped locomotor patterns, such as walking and swimming, but resulted in selective defects in skilled locomotion. We observed an increase of foot slips and falls at the balance beam and the horizontal ladder, indicating that elimination of CSF-cN leads to defects in adaptive motor control. Surprisingly, we found that in mice Pkd2l1 activity is dispensable for CSF-cN function. However, elimination of CSF-cN cilium is sufficient to completely recapitulate the phenotypes observed after neuronal ablation, thus demonstrating that this structure is necessary for sensory transduction. These findings indicate that during the evolutionary transition from swimming to walking, CSF-cN have acquired a novel role in order to adapt to the specific needs of limbed-based locomotion, and are an essential part of the sensory feedback mechanisms that contribute to adaptive motor control required for skilled locomotion.

Results

CSF-cN connect to key components of spinal motor circuits

We studied the physiological role of CSF-cN in the mammalian nervous system by obtaining genetic access using the *Pkd2l1::Cre* mouse line[18]. We verified targeting specificity by lineage tracing with a nuclear GFP reporter line[19] (*RosaΦHTB*) and found that at all spinal levels ~ 84% of labelled cells were Pkd2l1$^+$ and presented the characteristic position and morphology of CSF-cN (Figures S1A and S1B). In addition, we did not observe reporter expression in any other cell type in the central nervous system (Figure S1C).

In order to explore CSF-cN connectivity, we first investigated synaptic targets by labelling pre-synaptic boutons with tdTomato-tagged synaptophysin[20] (*Ai34*). We observed dense signal localized around the central canal and in the ventromedial part of the spinal cord at all axial levels (Figure 1A). Interestingly, key components of spinal motor circuits are characterized by stereotyped positioning in these areas along the entire rostro-caudal extent of the spinal cord. Median motor column (MMC) neurons controlling the activity of epaxial muscles are found in ventromedial location, while V0c neurons, cholinergic premotor interneurons, are positioned in the intermediate spinal cord in proximity to the central canal[21,22]. Thus, we asked whether MMC and V0c neurons receive synaptic input from CSF-cN. To test this hypothesis, we relied on the cholinergic nature and stereotyped position of these cell types to identify them (Figure 1B). We found putative synaptic contacts on ~57% of V0c and ~35% of MMC neurons at all spinal levels, as well as few instances of tdTomato$^+$ boutons juxtaposed to lateral motor column (LMC) neurons at lumbar and cervical levels (~13%; Figures 1C and S1D). In addition, we investigated whether other cardinal ventral interneuron subtypes represent possible synaptic targets of CSF-cN. We found synaptic boutons in close proximity of Lhx1$^+$ (V0/dI4)[23] and Chx10$^+$ (V2a)[24] interneurons, but not onto FoxP2$^+$ (V1)[25] and calbindin$^+$ ventral horn interneurons (Renshaw cells)[26] (Figure 1D). Altogether, these data

107 show that CSF-cN presynaptic terminals are found juxtaposed to key components of spinal
108 motor circuits.

109 To confirm the anatomical findings and assess functional connectivity, we expressed
110 channelrhodopsin-2[27] (ChR2, *Ai32*) in CSF-cN and used whole-cell patch-clamp recording
111 combined to ChR2-Assisted Circuit Mapping[28] (CRACM) to identify putative CSF-cN
112 postsynaptic partners. First, to validate the optogenetic model in CSF-cN, we carried out a set
113 of tests and our data show that in voltage clamp mode (V_h -90 mV) reliable photocurrents with
114 the characteristic properties - current with an initial transient and subsequent persistent phase
115 - can be elicited in CSF-cN with light pulse power set at 2 $mW.mm^{-2}$ (-150 and -65 pA for peak
116 and steady state currents, respectively) with little changes in amplitude with further increase in
117 power (Figures S2A and S2B; n=12 to 16). Thus, to ensure reliable ChR2 activation, we used
118 a power set at 5 $mW.mm^{-2}$. The analysis of the photocurrent current-voltage relationship (V_h -
119 70 mV and V_{Step} from -90 to -10 mV, 20 mV increments) indicates that the current amplitude
120 follows a linear regression with a current reversion at -10 mV (Figure S2C; n=67). Further, we
121 show that the photocurrents elicited with either repetitive light pulses (Figure S2D; n=8) or
122 with pulses of increased duration (Figure S2E; n=11) remained stable. Finally, we compared
123 the action potential (AP) discharge pattern induced in the same CSF-cN (current clamp mode
124 at RMP) either following positive DC current injection (+20 pA) or exposure to light pulses of
125 increasing duration and show that both stimuli triggered comparable spiking and AP discharge
126 frequency (Figure S2F; n=7) and that repetitive short light pulses reliably induced spiking over
127 time (Figure S2G). Taken together these data indicate that optical stimulation reliably
128 generated ChR2 photocurrents and evoked AP discharge in $ChR2^+$ CSF-cN.

129 Next, we recorded neurons to demonstrate functional connectivity between CSF-cN
130 and spinal interneurons. We focused on interneurons located close to the central canal (50 ± 5
131 µm; n=20. Figure 2C) in the proximity of $ChR2^+$ varicosities and determined their intrinsic

electrophysiological, firing, and morphological properties (Figure 2A). The majority of the recorded interneurons (15/20) presented electrophysiological (r_m: 541 ± 7 MΩ; c_m: 26 ± 2 pF), AP (AP half width: 2.0 ± 0.2 ms; discharge frequency: 26 ± 2 Hz, +50 pA DC current injection) and morphological properties compatible with V0c neurons identity[22] (Figures 2B and 2C). The remaining cells (5/20) were characterized by a different physiological profile suggesting that at least another interneuron subtype residing next to the central canal receive direct input from CSF-cN (Data not shown). In line with the neurotrasmitter phenotype of CSF-cN, we found that short light pulses evoked inward inhibitory responses in these neurons (V_h -70 mV and E_{Cl} -60 mV; 20/500 neurons patched) that were completely abolished in the presence of Gabazine (Figures 2D and 2E; n=20). Thus, physiological analysis confirms functional connectivity between CSF-cN and spinal interneurons positioned around the central canal.

CSF-cN are reciprocally connected and receive sparse input from spinal interneurons

Next, we explored sources of presynaptic input to CSF-cN by using rabies virus (RV) retrograde monosynaptic tracing[29]. We selectively targeted CSF-cN for rabies infection and transsynaptic spread by injecting a mixture of Cre-dependent helper adeno-associated viruses at lumbar (L) level 1 of *Pkd2l1::Cre* mice (AAV-syn-FLEX-splitTVA-EGFP-tTA and AAV-TREtight-mTagBFP2-B19G[30]). Three weeks later, EnvA pseudotyped G-deficient RV (RVΔG-mCherry/EnvA) was delivered at the same level (Figure 3A). We first examined starter cells, defined as neurons infected by both AAV and RV, and found BFP^+; RV^+ neurons around the central canal at the point of injection, with morphologies and positions characteristic of CSF-cN (Figures 3B-D). We next focused on transynaptically labelled neurons and found that the majority of BFP^-; RV^+ cells were also CSF-cN (~ 85%), but mainly located at more caudal levels of the spinal cord, thus indicating that CSF-cN are reciprocally connected, with caudal neurons sending input to rostral segments (Figures 3D and S3A-C). To further investigate

157 whether CSF-cN make ascending axonal projections, as suggested by rabies tracing
158 experiments and previously shown in zebrafish[31], we drove expression of TVA in CSF-cN at
159 L1 by focal injection of AAV-FLEX-TVAmCherry in *Pkd2l1::Cre* mice and then probed the
160 directionality of CSF-cN axons by delivering RVΔG-GFP/EnvA, either at a rostral (T10) or a
161 caudal (L3) level (Figures 3F and 3G). We observed retrograde infection of TVA expressing
162 CSF-cN only after rabies injection at T10, thus indicating that CSF-cN send axons only to more
163 rostral segmental levels (Figures 3F and 3G). Finally, we assessed whether CSF-cN form
164 functional reciprocal synaptic contact. By using CRACM, CSF-cN were recorded in voltage
165 clamp mode (V_h 0 mV) at the ChR2 current reversal potential to avoid recording contamination
166 with the photocurrent (Figures 3H and S2C). We show that exposure to short light pulses
167 evoked synaptic responses in all recorded CSF-cN (19/19). Moreover, these synaptic currents
168 were outward and completely abolished in the presence of Gabazine and Picrotoxin (Figures
169 3I and 3J; n=19) as expected for the chloride equilibrium potential (E_{Cl}) set at -60 mV and the
170 activation of $GABA_A$ receptors.
171 The remaining presynaptic input consisted of sparse labeling of spinal interneurons
172 without any distinct positional organization (Figures 3C-E). We analyzed the neurotransmitter
173 phenotype of CSF-cN presynaptic partners by assessing expression of *VGAT* and *VGLUT2* and
174 found that the majority of presynaptic neurons were $VGAT^+$, including CSF-cN that are known
175 to have GABAergic phenotype[32] (Figures S3D and S3E). Altogether, these data indicates that
176 CSF-cN are reciprocally connected and receive sparse input mainly by local inhibitory
177 interneurons.
178
179 ***CSF-cN are required for skilled locomotion***
180 Next, to study the function of CSF-cN in motor control, we crossed the *Pkd2l1::Cre*
181 line with the *RosaΦDTR* allele to drive expression of the diphtheria toxin receptor[33] (DTR).

Diphtheria toxin (DT) administration in adult mice resulted in elimination of >80% CSF-cN within two weeks (Figures 4A, 4B, S4A, and S4B). We first evaluated the effect of acute ablation of CSF-cN on general locomotor function associated with exploratory behavior by using the open field test. We did not find any significant difference between DT- and PBS-treated mice in activity, speed, distance travelled, and turning behavior (Figures 4C-E, and S4G). Next, we performed kinematic analysis on freely walking mice to evaluate gait and did not observe any effect on step cycle, step length, base of support, body stability, and the precision of foot placement, key parameters describing limb movement and coordination during unperturbed locomotion[34] (Figures 4F, 4G, S4C, S4H, S5 and Video S1). These data show that elimination of CSF-cN does not affect activity or generation of the patterns and rhythms of muscle contraction necessary for walking gait in mice. In larval zebrafish, CSF-cN have been shown to have an important role for postural control[11]. Thus, we evaluated tasks requiring control of trunk position and stability. First, we scored spontaneous rearing events, and found no effect of CSF-cN ablation on rearing duration and frequency (Figure S4D and data not shown). Second, we tested swimming, a locomotor behavior that requires coordination of limbs and trunk in order to obtain directional movements[35]. We did not observe any difference in speed or in the angle between the trunk and the water line, an indicator of postural control[36] (Figures S4E, S4F, and Video S2). These experiments show that elimination of CSF-cN does not perturb postural control.

Finally, we tested skilled locomotion by assessing performance at the balance beam and horizontal ladder, tasks that are known to require precise sensory feedback in order to achieve accuracy in foot placement[37]. We used beams and ladders of different widths and rung spacing in order to assess the effect of progressively more difficult conditions[1]. In both tasks, DT-treated mice presented clear deficits in motor performance (Videos S3 and S4) that resulted in an increase in the numbers of foot slips and falls, which was significantly higher than control

207 animals in the more challenging configurations (Figures 4H and 4I). Thus, these data indicate
208 that CSF-cN are required for skilled locomotion.
209
210 ***The cilium is necessary for CSF-cN function***
211 Next, we wondered whether the Pkd2l1 channel is necessary for CSF-cN function in
212 mice, as in zebrafish its elimination impairs mechanosensation and behavioral responses to
213 changes in spinal bending[12,15]. To address this question, we analyzed locomotor behavior in
214 Pkd2l1 knockout mice[38] (*Pkd2l1-/-*; Figure 5A). In line with the results obtained after neuronal
215 ablation experiments these mice did not show any phenotype at the open field, gait analysis,
216 and swimming tests (Figures 5B-D, S5, and data not shown; Videos S1 and S2). Surprisingly,
217 *Pkd2l1-/-* mice performance at the balance beam and horizontal ladder was also
218 indistinguishable from control mice (Figures 5E and 5F; Videos S3 and S4). Altogether these
219 data suggests that CSF-cN function in mice does not require Pkd2l1 activity.
220 Cilia have been known to function as a mechanosensory organelle responding to fluid
221 flow in many different cell types and most notably in sensory neurons. The intraflagellar
222 transporter 88 (Ift88) is part of the Ift-B complex that is crucial for transport of ciliary proteins
223 and its elimination suppress ciliogenesis[39]. Thus, to study the consequences of preventing
224 cilium formation in CSF-cN, we crossed the *Pkd2l1::Cre* allele with the conditional *Ift88*^{fl}
225 mouse line[40] (*Pkd2l1::Cre +/-; Ift88*$^{fl/fl}$, hereafter referred to as Δ*Cilia*). We first confirmed
226 success of this strategy by visualizing CSF-cN protrusions in the central canal and the
227 associated cilium. In control animals, we found that >70% of Pkd2l1^{+} apical processes
228 presented a cilium, while in Δ*Cilia* mice we found a significant reduction in the occurrence of
229 ciliated CSF-cN (~35%; Figures 6A and 6B). Moreover, electron microscopy analysis
230 confirmed that conditional elimination of Ift88 prevents ciliogenesis in CSF-cN (Figure 6C).
231 Next, we evaluated locomotor behavior in Δ*Cilia* mice. We did not observe any significant

defect in the open field, gait analysis, and swimming tests (Figures 6D-G, S5, and S6; Videos S1 and S2). In contrast, the performance of Δ*Cilia* mice at the balance beam and horizontal ladder was perturbed (Videos S3 and S4). Strikingly, quantification of foot slips and foot falls revealed that Δ*Cilia* made significantly more mistakes when walking on the more challenging versions of the tests, thus precisely recapitulating the phenotype observed after CSF-cN ablation (Figures 6H and 6I). Altogether these data show that the behavioural defects observed after elimination of the cilium phenocopy the ones occurring after neuronal ablation, thus indicating that this structure is necessary for CSF-cN function in motor control in mice.

Discussion

In this study we investigated the physiological role of CSF-cN, an evolutionary conserved vertebrate sensory system, in limbed mammals. We found that these neurons are integrated into spinal motor circuits and contribute to adaptive motor control necessary for skilled locomotion. CSF-cN function in mice does not require the activity of the Pkd2l1 channel but entirely depends on its cilium, thus pointing to a key role for this mechanosensory structure in monitoring CSF flow. Altogether, our data suggests a model where CSF-cN provide an additional source of proprioceptive information by monitoring spinal curvature and represent an integral component of the sensory feedback mechanisms necessary for adaptive motor control.

Kolmer and Agduhr first described a peculiar population of sensory neurons lining the central canal and proposed that they constitute a sensory organ relaying information from the CSF[4,5]. CSF-cN function has remained elusive until recent studies in lamprey and zebrafish revealed important roles in modulation of swimming and postural control[10,12,13]. CSF-cN have been shown to provide information to the motor system about active and passive curvature of the body axis by sensing fluid flow along the central canal[12,15,41]. In fish, the importance of monitoring curvature along the rostro-caudal axis of the spinal cord is clear, as swimming relies on the rhythmic propagation of an undulatory pattern of muscle contraction. The introduction of limbs has led to the reorganization of motor circuits in order to accommodate the biomechanical requirements of terrestrial locomotion[17]. The coordination of limb movements and precision of foot placement represent a critical feature of motor control in over ground locomotion[42]. In particular, it is especially important for navigating the diverse terrains and obstacles animals are confronted with in the wild and require dynamic integration of different sources of sensory information[37]. In our experiments, we observed that locomotor patterns and rhythms, as well as the accuracy of foot placement is not affected during unperturbed

locomotion on a plexiglass runway. However, under more challenging conditions at the balance beam and horizontal ladder, where movements need to be more precisely controlled we found a significant increase in the number of foot slips and falls. CSF-cN, by sensing spinal bending, can provide an extra layer of proprioceptive information that is dispensable during normal locomotion but required for skilled locomotion. Thus, a sensory system modulating wave-like movements at the basis of swimming in fish may have evolved a novel role in the control of adaptive motor responses necessary to precisely regulate limb and body movements in limbed vertebrates.

At circuit level, we observed input-output connectivity patterns that are consistent with CSF-cN physiological role in sensorimotor integration. We found CSF-cN presynaptic puncta on motor neurons, thus possibly providing a direct way to regulate motor output, and on cardinal ventral interneuron subtypes such as $ChAT^{+}$ V0c , $Lhx1^{+}$ V0/dI4, and $Chx10^{+}$ V2a interneurons, indicating connectivity to key components of spinal premotor circuits. At physiological level, we confirmed that CSF-cN make functional inhibitory connections with spinal interneurons located around the central canal. However, we could not record functional connections to motor neurons. This discrepancy with the anatomical findings could be due to sparse connectivity and the technical limitation of finding intact connections in spinal cord coronal slices. In terms of input connectivity to CSF-cN, rabies monosynaptic tracing experiments revealed inputs from local spinal interneurons mostly of inhibitory character. Presynaptic inhibition could control the gain of CSF-cN activity, a well-known mechanism for tuning somatosensory feedback in spinal circuits[43]. In addition, we observed abundant recurrent connectivity between CSF-cN, with neurons located at caudal spinal segments sending ascending input to ones at more rostral levels. Zebrafish CSF-cN have been shown to form ascending axonal projections[44] and prominent bilateral CSF-cN axonal bundles can be found in the medial aspects of the ventral white matter in mice (Video S5). An inhibitory

feedback loop from posterior to anterior CSF-cN is well suited for coordination of undulatory movements in fish, but its significance for limb-based locomotion remains to be explored.

At behavioral level, our data show that in mice elimination of CSF-cN does not perturb general motor activity and the generation of rhythmic patterns of limb movement necessary for the production of stereotyped locomotor actions, such as walking and swimming. In contrast, we observe an increase of foot slips and falls at the balance beam and horizontal ladder, indicating that the precision in motor control required for performing skilled movements is perturbed. Interestingly, the effect is significant only in the most challenging versions of the tasks. These data support the idea that multiple sources of sensory information, including cutaneous and muscle afferents, the visual, and the vestibular systems, are integrated to precisely adjust limb and body movements in order to prevent foot slippage during the execution of skilled actions and suggest that CSF-cN may provide proprioceptive information about body position[1]. Previous work in lamprey and zebrafish, along with our observation that elimination of the cilium completely recapitulates the defects observed after neuronal ablation, point to a role for CSF-cN in mice as mechanoreceptive sensory neurons detecting curvature of the spinal cord by sensing CSF flow in the central canal[41]. Thus, we propose that CSF-cN by monitoring spinal bending provide additional proprioceptive feedback informing the motor system on axial position that is used to adjust trunk and limb movement during locomotion. Walking on narrow paths or challenging terrains introduces forward and lateral displacements in the body axis that can be finely monitored by CSF-cN. For example, walking on a balance beam reduces lateral stability by decreasing the available base of support or walking on the horizontal ladder requires to overextend hindlimbs in order to land on the same rung where the forelimbs touched down, thus resulting in exaggerated hip torsion[37].

Surprisingly we did not observe any defect in locomotor behavior upon elimination of Pkd2l1. This is in contrast with its requirement for CSF-cN function in zebrafish, thus raising

interesting questions regarding additional molecular effectors in mammals. Our study does not exclude the possibility that in mice Pkd2l1 might be selectively required for chemosensation, as this channel has been shown to respond directly to pH changes[8]. The ability to monitor CSF composition has been proposed to be part of a homeostatic mechanisms common to all vertebrates for counteracting the effects of pH changes by reducing muscle activity[14]. It will be interesting to address whether chemosensation in mammalian CSF-cN could serve as system for modulating motor behavior in response to changes in the internal state of the animal, for example in case of fatigue or sickness.

Altogether, our anatomical and functional data indicate that CSF-cN are an important component of sensorimotor circuits in the mammalian spinal cord contributing to adaptive motor control. This study opens the way for future work to address exciting questions on how information on CSF composition and flow is encoded by CSF-cN and integrated at a circuit level with other sensory input, such as muscle and cutaneous feedback, in order to orchestrate flawless execution of motor programs.

Acknowledgements

We thank Liana Kosizki for technical support and the MDC Advanced Light Microscope facility for assistance with image acquisition and analysis. Sofia Pimpinella for helping with spinal injections and Pierre-Louis Ruffault for advice with experimental design; We thank Robert Manteufel, Ilka Duckert, and Florian Keim for animal care; Baptiste Lasbats and Lilly von Kalckreuth for assistance with behavioral experiments; Nikos Balaskas, Marco Beato, Joriene De Nooij, and members of the Zampieri laboratory for insightful comments on the manuscript. N.Z. and NW were supported by a DFG-ANR international collaborative grant (MotAct-CSF. DFG ZA 885/1-2; ANR-16-CE92-0043); N.W. by AMU and CNRS INSB.

Author contributions

Conceptualization, K.G., N.W., and N.Z.; Investigation, K.G., N.J., E.B., S.K., and F.S.; Formal analysis, K.G., N.J., E.B and S.K.; Writing – Original Draft, K.G. and N.Z.; Writing – Review and Editing, K.G., N.W., and N.Z.; Supervision, N.W. and N.Z.

Declaration of interests

The authors declare no competing interests.

Figure Titles and Legends

Figure 1. CSF-cN project to key components of spinal motor circuits.

A) Representative images of synaptophysin-tdTomato labeling of CSF-cN at cervical, thoracic and lumbar levels of P7 *Pkd2l1::Cre; Ai34* mice. Arrows point to dense labeling nearby the central canal and the ventromedial area of the spinal cord.

B) Representative images of synaptophysin-tdTomato puncta in close contact with $ChAT^+$ V0c and MMC neurons at thoracic level of P7 *Pkd2l1::Cre; Ai34* mice. Magnifications show single z-planes.

C) Proportion of V0c, MMC, and LMC neurons that receive synaptic input from CSF-cN at cervical, thoracic and lumbar levels (n=3).

D) Representative images of synaptophysin-tdTomato puncta in close contact with ventral interneurons subtypes. We found $Tomato^+$ puncta on $Lhx1^+$ (V0/dI4) and $Chx10^+$ (V2a) interneurons, but not onto $FoxP2^+$ (V1) and $calbindin^+$ ventral horn interneurons (Renshaw cells) . Scale bar: 200 µm. Magnifications show single z-planes.

See also Figure S1 and Video S5.

Figure 2. CSF-cN form functional synaptic contact with spinal interneurons

A) Schematic of patch-clamp recordings and ChR2-assisted circuit mapping to identify putative CSF-cN postsynaptic partners.

B) Micrographs showing a responsive interneuron position (arrow, IR-DIC) and its morphology (green, Alexa488 dialysis during recording, scale bar: 20 µm). Right, traces showing the electrophysiological properties of the interneurons shown on the left. Recording in current clamp at RMP -73 mV and injection of DC current steps from -90 to +50 pA

(increments: +20 pA) showing a large hyperpolarization and sustained high frequency AP discharge upon negative and positive direct current injection, respectively.

C) Schematic (left) illustrating parameters used for quantifying .the position (center) and size (right) of responsive neurons (n=20; mean ± SD).

D) Representative traces of the photo-evoked inward currents recorded in one interneuron (voltage clamp mode, V_h -70 mV and E_{Cl} -60 mV) upon repetitive optical activation (10 ms, 5 $mW.mm^{-2}$ every 500 ms, see LED pulse under the traces) of $ChR2^+$ CSF-cN terminals present on the neuron. Top: recording in the presence of 1 µM Strychnine and 20 µM DNQX, Bottom: addition to the bath of 10 µM Gabazine (Gbz) completely blocks the evoked responses. Traces are the average of 5 consecutive recordings and the inset on the right show individual responses for the first light pulse.

E) Summary box-whisker plot for IPSC current amplitude in control (blue box, CTR), in the presence of Strychnine and DNQX alone (grey box, SD), and with Gabazine added to the bath (red box, SDG). (Kruskal Wallis Test: χ^2=62,589, df=2, p=$2.564.10^{-14}$; Post-hoc Wilcoxon pairwise test: CTR vs SD, p=0.32; CTR and SD vs. SDG, p=$1.3.10^{-13}$ and p=2.10^{-6}, respectively; n=20).

See also Figure S2.

Figure 3. CSF-cN are reciprocally connected and receive sparse input from local spinal interneurons.

A) Schematic illustrating rabies monosynaptic tracing approach to identify cells providing input to CSF-cN. A mix of Cre-dependent helper AAVs driving the expression of TVA and G was injected at L1 of P7 *Pkd2l1::Cre* mice. Three weeks later, RVΔG-mCherry/EnvA was injected at the same position and after 7 days spinal cords were examined.

B) Representative images of BFP^+; RV^+ starter cells and BFP^-; RV^+ second order CSF-cN. Scale bar: 20 µm.

C-D) Digital reconstruction of medio-lateral/dorso-ventral position (C) and medio-lateral/rostro-caudal position (D, thoracic segment on top) of starter cells (blue) and second order cells (red); n=3.

E) Representative images of second order neurons labeled in rabies tracing experiments from CSF-cN.

F) Schematic illustration of retrograde tracing approach to test directionality of CSF-cN axonal projections. Injection of AAV-FLEX-TVAmCherry in *Pkd2l1::Cre* mice at P7 was followed three weeks after by RVΔG-GFP/EnvA injection at T10. Representative image shows AAV^+/RV^- and AAV^+/RV^+ cells at L1.

G) Schematic illustration of retrograde tracing approach to test directionality of CSF-cN axonal projections. Injection of AAV-FLEX-TVAmCherry in *Pkd2l1::Cre* mice at P7 was followed three weeks by RVΔG-GFP/EnvA injection at L3. Representative image shows AAV^+/RV^- cells at L1, no RV^+ cells were detected.

H) Representative epifluorescence image of one $ChR2^+$ CSF-cN recorded in an acute lumbar spinal cord slice (250 µm, cc: central canal) obtained from a *Pkd2l1::Cre; RosaΦChrR2* mice showing ChR2 expression through YFP (Top) and Alexa 594 fluorescence (Bottom) upon cell dialysis through the patch pipette. Right, voltage-dependance of the ChR2 photo-evoked current in CSF-cN recorded in voltage clamp mode (V_h -70 mV) at the voltage potential steps indicated under the traces. Note the decrease in the photocurrent amplitude with depolarizing voltage steps (null for -10 mV, see also Figure S2C) and the presence of currents (*) that develop shortly after the onset of the photocurrent and are either inward for potential hyperpolarized or outward for potentials more depolarized than -60 mV (E_{Cl}), respectively.

I) Representative traces of the photo-evoked outward currents recorded in one CSF-cN (voltage clamp mode, V_h 0 mV and E_{Cl} -60 mV) upon repetitive optical activation (10 ms, 5 mW.mm^{-2} every 500 ms, see LED pulse under the traces) of ChR2$^+$ CSF-cN terminals present on the neuron. Top: control condition. Bottom: 100 µM Picrotoxin (Ptx) and 10 µM Gabazin (Gbz) blocked the evoked responses. The traces illustrated are the average of 5 consecutive recordings and the inset on the right shows for the first light pulse individual responses.

J) Summary box-whisker plot for IPSC current amplitude in control (CTR) and in the presence Gbz and Ptx. (Wilcoxon signed rank Test: p=0.00013; n=19).

See also Figure S3.

Figure 4. Pharmacological ablation of CSF-cN perturbs skilled locomotion.

A) Representative images of Pkd2l1$^+$ neurons around the central canal 60 days after PBS (left) or DT (right) injection in *Pkd2l1::Cre; RosaΦDTR* mice.

B) Quantification of Pkdl21$^+$ neurons around the central canal 60 days after PBS (n=3) or DT (n=3) injection in *Pkd2l1::Cre; RosaΦDTR* mice.

C-E) Locomotor activity during a 90 min open field test. Percentage of time spent moving (C), speed (D) and distance traveled (E) in adult *Pkd2l1::Cre; RosaΦDTR* mice 14 days after PBS (n=8) or DT (n=6) treatment.

F) Step cycle in adult *Pkd2l1::Cre; RosaΦDTR* mice 14 days after PBS (n=6) or DT (n=6) treatment.

G) Step length in adult *Pkd2l1::Cre; RosaΦDTR* mice 14 days after PBS (n=6) or DT (n=6) treatment (LF left forelimb, LH left hindlimb, RF right forelimb, RH right hindlimb).

H) Quantification of foot placement errors (slips and falls) in the balance beam test with 2 cm (left) or 1 cm (right) beam width in adult *Pkd2l1::Cre; RosaΦDTR* mice 14 days after PBS (n=6) or DT-injection (n=5).

I) Quantifications of foot placement errors (slips and falls) in the horizontal ladder test with 1 cm (left) or 2 cm (right) rung distance in adult *Pkd2l1::Cre; RosaΦDTR* mice 14 days after PBS (n=6) or DT-injection (n=6).

Mean±SEM, paired t-test, ns $p>0.05$, ** $p<0.01$, *** $p<0.001$.

See also Figure S4, S5, and Video S1-S4.

Figure 5. Pkd2l1 elimination does not affect locomotion.

A) Representative images of Pkd2l1 staining in adult *Pkd2l1* +/+ and *Pkd2l1* -/- animals.

B) Percentage of moving time in adult *Pkd2l1* +/+ (n=8) and *Pkd2l1* -/- (n=9) during 90 min open field test.

C) Step cycle of forelimbs (top) and hindlimbs (bottom) in adult *Pkd2l1* +/+ (n=8) and *Pkd2l1* -/- (n=9).

D) Analysis of turning behavior (total, clockwise, and counterclockwise turns) during a 90 min open field test in adult *Pkd2l1* +/+ (n=8) and *Pkd2l1* -/- (n=9) mice.

E) Quantification of foot placement errors (slips and falls) in the balance beam test with 2 cm (left) or 1 cm (right) beam width in adult *Pkd2l1* +/+ (n=8) and *Pkd2l1* -/- (n=10).

F) Quantification of foot placement errors (slips and falls) in the horizontal ladder test with 1 cm (left) or 2 cm (right) rung distance in adult *Pkd2l1* +/+ (n=8) and *Pkd2l1* -/- (n=10).

Mean±SEM; paired t-test, ns $p>0.05$.

See also Figure S5 and Video S1-S4.

Figure 6. Elimination of CSF-cN cilium phenocopies neuronal ablation.

A) Representative images of Pkd2l1$^+$ CSF-cN apical protrusions and acetylated-Tubulin$^+$ cilia in adult *control* and Δ*cilia* mice. High magnifications of Pkd2l1$^+$ protrusion in the central canal of *control* (A^I) and Δ*cilia* (A^{II}) mice.

B) Quantification of Pkd2l1^{+} CSF-cN apical protrusions bearing an acetylated-Tubulin^{+} cilium in *control* and Δ*cilia* mice (n=3).

C) Representative electron microscopy images of CSF-cN (highlighted in yellow) in *control* (left) and Δ*cilia* (right) mice. Arrow point to the cilium.

D) Average speed during a 90 min open field test in adult *control* (n=8) and Δ*cilia* (n=4) mice.

E) Percentage of moving time in adult *control* (n=7) and Δ*cilia* mice (n=4) during 90 min open field test.

F) Step cycle of forelimbs (top) and hindlimbs (bottom) in adult *control* (n=10) and Δ*cilia* mice (n=9).

G Quantification of trunk angle between body axis and water line during swimming task in adult *control* (n=10) and Δ*cilia* mice (n=9).

H Quantification of foot placement errors (slips and falls) in the balance beam test with 2 cm (left) or 1 cm (right) beam width in adult *control* (n=6) and Δ*cilia* mice (n=6).

I) Quantification of foot placement errors (slips and falls) in the horizontal ladder test with 1 cm (left) or 2 cm (right) rung distance in adult *control* (n=10) and Δ*cilia* mice (n=9).

Mean±SEM; paired t-test, ns $p>0.05$, ** $p<0.01$, *** $p < 0.001$.

See also Figure S5, S6, and Video S1-S4.

STAR METHODS

RESOURCE AVAILABILITY

Lead Contact

Further information and requests for resources and reagents should be directed to the lead contact, Niccolò Zampieri (niccolo.zampieri@mdc-berlin.de).

Material availability

All unique reagents generated in this study are available from the lead contact without restriction.

Data and code availability

This study did not generate any unique dataset or code.

Original data supporting the current study are available from the lead contact upon request.

All additional information required to reanalyze the data reported in this paper is available from the corresponding lead contact upon request.

EXPERIMENTAL MODEL AND SUBJECT DETAILS

Animal Experimentation Ethical Approval

All animal procedures were performed in accordance to European community Research Council Directives and were approved by the Regional Office for Health and Social Affaires Berlin (LAGeSo) under license number G148/17 and the French “Direction Départementale de la Protection des Populations des Bouches-du-Rhône” (Project License Nr: APAFIS 17596; 2018111919329153. N.W. and License for the Use of Transgenic Animal Models Nr: DUO-5214).

Animal models

Mice were bred and maintained under standard conditions on a 12h light/dark cycle with access to food and water *ad libitum*. The day of birth was considered as postnatal day 1 (P1).

METHODS DETAILS

Ablation of CSF-cNs

To specifically ablate CSF-cNs *in vivo*, diphtheria toxin (DT; Sigma D0564) was administered intraperitoneally (50 mg.Kg^{-1}) at P40. Ablation efficiency was verified by staining for Pkd2l1.

Behavioral experiments

Mice were placed in the behavior room 30 min before starting the experiments, allowing them to acclimatize. Both sexes were included and for each test at least two representative videos with continuous movements were analyzed. For the *open field* test we used the ActiMot Infrared light beam activity monitor (TSE Systems). Two light-beam frames allowed to monitor X, Y and Z coordinates of the mouse. Animals were placed in the associated squared acrylic glass boxes (40 cm X 20 cm) and after 10 min of habituation time, spontaneous movements were monitored for 90 min. Data were evaluated with TSE supplied software. *Gait analysis* was performed as previously described[45]. Briefly, mice were placed on a customized acrylic glass walkway with surrounded LED lights to generate the internal reflection effect. A mirror under the walkway allows tracking of footprints and body outline with a high-speed camera (shutter speed 5,56 ms, frame rate 150 f/sec). Representative videos with straight and continuous runs were analyzed using the open-source MouseWalker software. To evaluate balance, we used a customized *balance beam* with replaceable beams of different sizes. Animals were placed on one end and had to pass the beam spontaneously to reach a shelter on the other side. A mirror was placed underneath and a high-speed camera captured the passage.

The *horizontal ladder* was customized with side walls made of acrylic glass to create a walking path and inserted metal rungs with 3 mm diameter. Rungs had a minimum distance of 1 cm and spacing of the rungs were modified by removing individual rungs. A mirror under the horizontal ladder and the clear walls allowed tracking from the side and underneath with a high-speed camera. Animals were required to pass the walking floor spontaneously and videos with continuous runs were analyzed. For the *swim task*, a custom-build acrylic glass tank (10 cm X 70 cm) filled with ambient temperature water was used. Mice had to swim through the tank to reach a platform on the other end. A mirror underneath allowed monitoring swim movements with a high-speed camera. The angle between body axis and water line was obtained by using the open-source program DeepLabCut[46]. The algorithm was trained to extract coordinates of nose and tail base in all frames. A value of likelihood allowed to estimate the reliability of detected coordinates and only frames with a likelihood superior to 0.9 were used for further analysis. The x/z coordinates of indicated points allowed the calculation of the swim angle between waterline and body axis.

Perfusion and tissue preparation

Anesthesia was induced by the intraperitoneal injection of ketamine (120 mg/kg) and Xylazine (10 mg/kg). After testing the toe-pinch reflex, animals were intracardially perfused with 10 ml ice-cold PBS, followed by the perfusion of ice-cold 4 % PFA (pH 7.4). The spinal cords were exposed via laminectomy and post-fixed overnight in 4 % PFA (pH 7.4) at 4 °C. After washing for 5 min in PBS, tissue was incubated in 30% sucrose over night at 4 °C for cryoprotection. Samples were embedded in Optimal Cutting Temperature (O.C.T., Tissue-Tek) compound, frozen on dry ice and stored at -80 °C.

Slice preparation, electrophysiology and optogenetic stimulation.

561 *Pkd2l1::Cre*; *Rosa-Φ-ChR2*(Ai32) or *Pkd2l1::Cre; Rosa-Φ-ChR2*(Ai32); *Rosa-Φ- Rosa-Φ-*
562 *tdTomato*(Ai14) mice (2-4 week-old) were anesthetized with an intraperitoneal injection of a
563 Ketamine/xylazine mixture (120/10 mg.Kg-^{1}) and perfused intracardiacally (>3-week-old)
564 with an ice cold and oxygenated (95% O_2/5% CO_2) modified artificial cerebrospinal fluid
565 (aCSF, in mM: NaCl 75, NaH_2PO_4 1.25, $NaHCO_3$ 33, KCl 3, $MgSO_4$ 7, sucrose 58, glucose
566 15, ascorbic acid 2, myo-inositol 3, sodium pyruvate 2, $CaCl_2$ 0.5, pH 7.4, 310 mosmol.Kg^{-1}).
567 Following laminectomy and spinal cord extraction, lumbar spinal cord coronal slices (250 to
568 300 µm) were prepared, transferred in a submerged incubation chamber filled with oxygenated
569 aCSF (in mM: NaCl 115, NaH_2PO_4 1.25, $NaHCO_3$ 26, KCl 3, $MgSO_4$ 2, glucose 15, ascorbic
570 acid 2, myo-inositol 3, sodium pyruvate 2, $CaCl_2$ 2; pH 7.4, 300 mosmol.Kg-1) at 35° C for 15
571 min and subsequently at room temperature (20-25°C) until use. For recording, slices were
572 transferred in the perfusion chamber (aCSF 2-4 mL.min^{-1}, 20-25°C) under an epifluorescence
573 upright microscope equipped with a CCD camera (HQ2 CoolSnap, Photometrics). Electrodes
574 (3-6 MΩ, borosilicate glass, Harvard Apparatus) were filled with a solution containing (in
575 mM): K-gluconate 120, NaCl 5, HEPES 10, $MgCl_2$ 1, $CaCl_2$ 0.25, EGTA 2, Mg-ATP 4, Na_2-
576 phosphocreatine 10, Na_3-GTP 0.2 (pH 7.3, 295 mosmol.kg-1 and a chloride equilibrium
577 potential (E_{Cl}) set at -60 mV) and 20 µM AlexaFluor488 (Invitrogen). Neurons were identified
578 in slices under infra-red DIC illumination (IR-DIC) and recorded in whole-cell patch-clamp
579 configuration performed in voltage- (VC) and current-clamp (CC) modes using a MultiClamp
580 700B amplifier (Molecular Device Inc.). Data were filtered at 2–2.4 kHz and digitized at 10
581 kHz using a Digidata 1322A interface driven by pClamp 9.2 (Molecular Device Inc.). Neuron
582 intrinsic and firing properties were determined using -10 mV voltage steps (V_{Step}) from a
583 holding potential (V_h) of -70 mV (VC) or current injection pulses (CC) from the resting
584 membrane potential (RMP). Validation of the optogenetic approach was performed by
585 recording Channelrhodopsin-2 (ChR2) expressing CSF-cN in VC or CC mode and ChR2

586 activation elicited using light pulses delivered through the objective (60x, NA 0.9; pUltra 300
587 CoolLED: 490 nm, with controlled power and duration). CSF-cN were recorded either in VC
588 mode (V_h -70 mV) to characterize ChR2 photocurrent properties and voltage-dependance (V_{Step}
589 from -90 to +10 mV, 200 ms at V_h -70 mV) or in CC mode at RMP to assess light-triggered
590 action potentials (APs) firing. Synaptic currents were photo-evoked in CSF-cN and
591 interneurons with 10 ms light pulses in control and in the presence of 1 µM strychnine (Sigma-
592 Aldrich), 20 µM DNQX either alone or with 10 µM gabazine and 100 µM picrotoxin (Gbz and
593 Ptx, BioTechne, UK) . In all recordings, the liquid junction potential was left uncorrected.
594
595 **Immunohistochemistry**
596 For histology, spinal cords were with a cryostat (Leica) collected on Superfrost Plus®
597 microscope slides (Thermo Fisher Scientific). Primary and secondary antibodies were diluted
598 in 4 % BSA in 0.3 % TritonX in PBS. Slides were mounted with Vectashield (Vector). The
599 following primary antibodies dilutions have been used: chicken anti-GFP (1/1000, Abcam),
600 goat anti-ChAT (1/200; Millipore), goat-anti FoxP2 (1/200, Abcam), mouse anti-acetylated
601 Tubulin (1/500, Sigma), rabbit anti-Calbindin (1/500, Swant), rabbit anti-dsRed (1/1000;
602 TaKaRa), rabbit anti-Lhx1(1/10000), generated in the Jessell laboratory), rabbit anti-Pkd2l1l
603 (1/200; Millipore), sheep anti-Chx10 (1/100, Abcam). Images were taken with a Zeiss LSM800
604 confocal laser scanning microscope.
605
606 **Viral tracings**
607 Intraspinal injections were performed as previously described (Zampieri et al., 2014). For
608 analgesia, mice were subcutaneously injected with 5 $mg.Kg^{-1}$ Carprofen 30 min before surgery.
609 Anesthesia was induced with continuous inhalation of isoflurane (2-3 %) in oxygen (1.5 %),
610 using an isoflurane vaporizer (Parkland Scientific). Dorsal laminectomy was performed to

611 expose the lumbar spinal cord prior to virus injection using a pulled borosilicate glass pipette
612 (World Precision Instruments, Inc.) and a micro syringe pump injector (Smart Touch). For
613 AAV, either a cocktail of AAV-TREtight-mTag BFP2-B19G ($4.48*10^{12}$ VG/mL) and AAV-
614 FLEX-SPLIT TVA-EGFP-tTA ($5.79*10^{10}$ VG/mL) was injected. A total amount of 300 nl of
615 virus was inoculated into two adjacent spots bilaterally 40 µm left and right to the midline.
616 After three weeks we performed intraspinal injection of 300 nl RVΔG(EnvA)-mCherry
617 ($1.94*10^{8}$ IU/mL) at the same position and animals were sacrificed seven days after. To analyze
618 directionality of CSF-cN projections, we injected AAV-FLEX-TVAmCherry ($5.33*10^{13}$
619 VG/mL) at L1, followed three weeks later by injection of RVΔG-GFP/EnvA ($2.13*10^{8}$ IU/mL)
620 either more caudally or rostrally. Mice which postmortem revealed low viral labeling or a
621 spread into the central canal were excluded from analysis.
622
623 **Fluorescent in situ hybridization**
624 For mRNA detection via multiplex RNAscope, a modified protocol from Advanced Cell
625 Diagnostics (ACD, 322360-USM) was used. Briefly, fixed spinal cord tissue was prepared and
626 sectioned as described before. Spinal sections were post-fixed in 4 % PFA (pH 7.4) at 4 °C for
627 15 min. After washing and dehydration (at 4 °C in 50%, 70% and 100% Ethanol), a
628 hydrophobic barrier was created around sections. After incubation with 3 % hydrogen peroxide
629 solution (H_2O_2) at RT for 15 min, Protease IV treatment followed for 30 min at RT. C2 and C3
630 probes were dilutes 1/50 in sample diluent and hybridized for 2 hours at 40°C in a humid
631 chamber in a HybEZ oven. For signal amplification and detection, the RNAscope 2.5 HD
632 Reagents Detection Kit-RED (ACD, 32360) was used according to the manufacturer's
633 instructions. After Detection of each channel, immunostaining was performed as described
634 before and slices were mounted with ProLong Gold.
635

636 **Positional analysis**

637 Three-dimensional positional analysis was performed as previously described[47]. Spinal cords
638 were sectioned in 40 µm slices and cartesian coordinates of spinal neurons per section were
639 obtained using the imaging software IMARIS. Data were normalized to account for differences
640 in spinal cord size and shape. The position of each neuron was digitally reconstructed by
641 plotting the data in 'R' (R Foundation for Statistical Computing, Vienna, Austria, 2005), using
642 a customized script. Correlation analysis have been done using the ''corrplot'' package to
643 calculates the comparability of experiments using the Pearson correlation coefficient. Datasets
644 were clustered hierarchically.

645

646 **Electron microscopy**

647 Mice were perfused with 4 % (w/v) paraformaldehyde in 0.1 M phosphate buffer. Spinal cord
648 was dissected and 2-3 mm^3 cubes were fixed by immersion in 4 % (w/v) paraformaldehyde
649 and 2.5% (v/v) glutaraldehyde in 0.1 M phosphate buffer for 2 hours at room temperature (RT).
650 Samples were postfixed with 1% (v/v) osmium tetroxide for 3 hours at RT, dehydrated in a
651 graded series of ethanol, and embedded in PolyBed® 812 resin (Polysciences, Germany).
652 Ultrathin sections (60-80 nm) were stained with uranyl acetate and lead citrate, and examined
653 at 80 kV with a Zeiss EM 910 electron microscope. Acquisition was done with a Quemesa
654 CCD camera using iTEM software (Emsis GmbH, Germany).

655

656 **Tissue clearing and light-sheet microscopy**

657 Mice were anesthetized and transcardially perfused as described above. Spinal cord was
658 extracted after ventral laminectomy and fixed in 4% PFA for 2 days at 4°C. Tissue clearing
659 was performed as previously described with modifications[48]. In short, tissue was transferred to
660 CUBIC1 (25 wt% Urea, 25 wt% N,N,N',N'-tetrakis(2-hydroxypropyl) ethylenediamine, 15

wt% Triton X-100) and incubated at 37°C shaking. Every other day CUBIC1 solution was exchanged until tissue appeared transparent (~ 4 days). Afterwards, samples were washed for 1 day with PBS at RT, refractive index matched with EasyIndex (LifeCanvas Technologies) at 37°C and imaged with the ZEISS Light-sheet Z.1. For image analysis and video rendering Arivis Vision 4D (Arivis AG) and Imaris (Oxford Instruments) was used.

QUANTIFICATION AND STATISTICAL ANALYSIS

For behavior experiments, mice were randomly allocated into different experimental groups and data have been randomized before analysis whenever possible. Quantifications represent the average of at least three biological replicates per condition. Each dot represents one animal and error bars in all figures represent mean ± SEM. For electrophysiological experiments, data are presented as mean ± standard deviation (SD) and graphs represent box-whisker plot using Tukey's method where single dots represent outliers. Because the data are not normally distributed (Shapiro-Wilk test), statistical significance was tested using non-parametric statistical tests: Wilcoxon signed-rank (comparison of two conditions within a group) or Kruskal-Wallis (χ^2, degree of freedom (df) and p-value, multiple comparisons, with a post-hoc pairwise comparisons using Wilcoxon rank sum test) tests. Number of samples (n) and the applied statistical test used for individual experiments are indicated in the figure legends. Significance was defined as * $p<0.05$; ** $p<0.01$; *** $p<0.001$. Statistical analyses were performed using Microsoft Excel, GraphPad Prism and RStudio statistics (Version 8, GraphPad Software, RStudio v1.1.456).

682 **VIDEO FILES**

683 Video S1. Representative video of control, DT-treated, *Δcilium*, and *Pkd2l1 -/-* mice walking
684 on a Plexiglas runaway. Related to Figures 4, 5, and 6.

685

686 Video S2. Representative video of control, DT-treated, *Δcilium*, and *Pkd2l1 -/-* mice
687 swimming. Related to Figures 4, 5, and 6.

688

689 Video S3. Representative video of control, DT-treated, *Δcilium*, and *Pkd2l1 -/-* mice walking
690 on a 1 cm diameter balance beam. Related to Figures 4, 5, and 6.

691

692 Video S4. Representative video of control, DT-treated, *Δcilium*, and *Pkd2l1 -/-* mice walking
693 on the 2 cm rung distance horizontal ladder. Related to Figures 4, 5, and 6.

694

695 Video S5. Light sheet imaging of Tomato^{+} CSF-cN in *Pkd2l1::Cre; Ai14* mice at cervical,
696 thoracic, and lumbar levels. Related to Figure 1.

References

1. Rossignol, S., Dubuc, R., and Gossard, J.-P. (2006). Dynamic Sensorimotor Interactions in Locomotion. Physiol. Rev. *86*, 89–154.
2. Koch, S.C. (2019). Motor task-selective spinal sensorimotor interneurons in mammalian circuits. Curr. Opin. Physiol. *8*, 129–135.
3. Tuthill, J.C., and Azim, E. (2018). Proprioception. Curr. Biol. *28*, R194–R203.
4. Kolmer, W. (1921). Das „Sagittalorgan“ der Wirbeltiere. Z. Anat. Entwicklungsgesch. *60*, 652–717.
5. Agduhr, E. (1922). Über ein zentrales Sinnesorgan (?) bei den Vertebraten. Z. Anat. Entwicklungsgesch. *66*, 223–360.
6. Vígh, B., Manzano e Silva, M.J., Frank, C.L., Vincze, C., Czirok, S.J., Szabó, a., Lukáts, a., and Szél, a. (2004). The system of cerebrospinal fluid-contacting neurons. Its supposed role in the nonsynaptic signal transmission of the brain. Histol. Histopathol. *19*, 607–628.
7. Stoeckel, M.-E., Uhl-Bronner, S., Hugel, S., Veinante, P., Klein, M.-J., Mutterer, J., Freund-Mercier, M.-J., and Schlichter, R. (2003). Cerebrospinal fluid-contacting neurons in the rat spinal cord, a ?-aminobutyric acidergic system expressing the P2X2 subunit of purinergic receptors, PSA-NCAM, and GAP-43 immunoreactivities: Light and electron microscopic study. J. Comp. Neurol. *457*, 159–174.
8. Orts-Del'Immagine, A., Seddik, R., Tell, F., Airault, C., Er-Raoui, G., Najimi, M., Trouslard, J., and Wanaverbecq, N. (2016). A single polycystic kidney disease 2-like 1 channel opening acts as a spike generator in cerebrospinal fluid-contacting neurons of adult mouse brainstem. Neuropharmacology *101*, 549–565.
9. Djenoune, L., Khabou, H., Joubert, F., Quan, F.B., Nunes Figueiredo, S., Bodineau, L., Del Bene, F., Burcklé, C., Tostivint, H., and Wyart, C. (2014). Investigation of spinal

cerebrospinal fluid-contacting neurons expressing PKD2L1: evidence for a conserved system from fish to primates. Front. Neuroanat. *8*, 26.

10. Fidelin, K., Djenoune, L., Stokes, C., Prendergast, A., Gomez, J., Baradel, A., Del Bene, F., and Wyart, C. (2015). State-dependent modulation of locomotion by GABAergic spinal sensory neurons. Curr. Biol. *25*, 3035–3047.

11. Hubbard, J.M., Böhm, U.L., Prendergast, A., Tseng, P.-E.B., Newman, M., Stokes, C., and Wyart, C. (2016). Intraspinal Sensory Neurons Provide Powerful Inhibition to Motor Circuits Ensuring Postural Control during Locomotion. Curr. Biol. *26*, 2841–2853.

12. Böhm, U.L., Prendergast, A., Djenoune, L., Figueiredo, S.N., Gomez, J., Stokes, C., Kaiser, S., Suster, M., Kawakami, K., Charpentier, M., et al. (2016). CSF-contacting neurons regulate locomotion by relaying mechanical stimuli to spinal circuits. Nat. Commun. *7*, 1–8.

13. Jalalvand, E., Robertson, B., Wallén, P., and Grillner, S. (2016). Ciliated neurons lining the central canal sense both fluid movement and pH through ASIC3. Nat. Commun. *7*, 10002.

14. Jalalvand, E., Robertson, B., Tostivint, H., Wallén, P., and Grillner, S. (2016). The Spinal Cord Has an Intrinsic System for the Control of pH. Curr. Biol. *26*, 1346–1351.

15. Sternberg, J.R., Prendergast, A.E., Brosse, L., Cantaut-Belarif, Y., Thouvenin, O., Orts-Del'Immagine, A., Castillo, L., Djenoune, L., Kurisu, S., McDearmid, J.R., et al. (2018). Pkd2l1 is required for mechanoception in cerebrospinal fluid-contacting neurons and maintenance of spine curvature. Nat. Commun. *9*, 1–10.

16. Orts-Del'Immagine, A., and Wyart, C. (2017). Cerebrospinal-fluid-contacting neurons. Curr. Biol. *27*, R1198–R1200.

17. Grillner, S., and Jessell, T.M. (2009). Measured motion: searching for simplicity in

spinal locomotor networks. Curr. Opin. Neurobiol. *19*, 572–586.

18. Ye, W., Chang, R.B., Bushman, J.D., Tu, Y.-H., Mulhall, E.M., Wilson, C.E., Cooper, A.J., Chick, W.S., Hill-Eubanks, D.C., Nelson, M.T., et al. (2015). The K + channel K IR 2.1 functions in tandem with proton influx to mediate sour taste transduction. Proc. Natl. Acad. Sci., 201514282.

19. Li, Y., Stam, F.J., Aimone, J.B., Goulding, M., Callaway, E.M., and Gage, F.H. (2013). Molecular layer perforant path-associated cells contribute to feed-forward inhibition in the adult dentate gyrus. Proc. Natl. Acad. Sci. *110*, 9106–9111.

20. Daigle, T.L., Madisen, L., Hage, T.A., Valley, M.T., Knoblich, U., Larsen, R.S., Takeno, M.M., Huang, L., Gu, H., Larsen, R., et al. (2018). A Suite of Transgenic Driver and Reporter Mouse Lines with Enhanced Brain-Cell-Type Targeting and Functionality. Cell *174*, 465-480.e22.

21. Dasen, J.S., and Jessell, T.M. (2009). Chapter Six Hox Networks and the Origins of Motor Neuron Diversity. In Current topics in developmental biology (Elsevier Inc.), pp. 169–200.

22. Zagoraiou, L., Akay, T., Martin, J.F., Brownstone, R.M., Jessell, T.M., Miles, G.B., Thomas, M., and Miles, G.B. (2009). A Cluster of Cholinergic Premotor Interneurons Modulates Mouse Locomotor Activity. Neuron *64*, 645–662.

23. Pillai, A., Mansouri, A., Behringer, R., Westphal, H., and Goulding, M. (2006). Lhx1 and Lhx5 maintain the inhibitory-neurotransmitter status of interneurons in the dorsal spinal cord. Development *134*, 357–366.

24. Al-Mosawie, A., Wilson, J.M., and Brownstone, R.M. (2007). Heterogeneity of V2-derived interneurons in the adult mouse spinal cord. Eur. J. Neurosci. *26*, 3003–3015.

25. Morikawa, Y., Hisaoka, T., and Senba, E. (2009). Characterization of Foxp2-expressing cells in the developing spinal cord. Neuroscience *162*, 1150–1162.

772 26. Bikoff, J.B., Gabitto, M.I., Rivard, A.F., Drobac, E., MacHado, T.A., Miri, A.,
773 Brenner-Morton, S., Famojure, E., Diaz, C., Alvarez, F.J., et al. (2016). Spinal
774 Inhibitory Interneuron Diversity Delineates Variant Motor Microcircuits. Cell *165*,
775 207–219.
776 27. Madisen, L., Mao, T., Koch, H., Zhuo, J.M., Berenyi, A., Fujisawa, S., Hsu, Y.W.A.,
777 Garcia, A.J., Gu, X., Zanella, S., et al. (2012). A toolbox of Cre-dependent optogenetic
778 transgenic mice for light-induced activation and silencing. Nat. Neurosci. *15*, 793–802.
779 28. Petreanu, L., Huber, D., Sobczyk, A., and Svoboda, K. (2007). Channelrhodopsin-2–
780 assisted circuit mapping of long-range callosal projections. Nat. Neurosci. *10*, 663–
781 668.
782 29. Wickersham, I.R., Lyon, D.C., Barnard, R.J.O.O., Mori, T., Finke, S., Conzelmann,
783 K.-K.K., Young, J.A.T.T., and Callaway, E.M. (2007). Monosynaptic restriction of
784 transsynaptic tracing from single, genetically targeted neurons. Neuron *53*, 639–47.
785 30. Lavin, T.K., Jin, L., Lea, N.E., and Wickersham, I.R. (2020). Monosynaptic Tracing
786 Success Depends Critically on Helper Virus Concentrations. Front. Synaptic Neurosci.
787 *12*.
788 31. Djenoune, L., Desban, L., Gomez, J., Sternberg, J.R., Prendergast, A., Langui, D.,
789 Quan, F.B., Marnas, H., Auer, T.O., Rio, J.-P.P., et al. (2017). The dual developmental
790 origin of spinal cerebrospinal fluid-contacting neurons gives rise to distinct functional
791 subtypes. Sci. Rep. *7*, 1–14.
792 32. Jurčić, N., Michelle, C., Trouslard, J., Wanaverbecq, N., and Kastner, A. (2021).
793 Evidence for PKD2L1-positive neurons distant from the central canal in the
794 ventromedial spinal cord and medulla of the adult mouse. Eur J Neurosci *54*, 4781–
795 4803.
796 33. Buch, T., Heppner, F.L., Tertilt, C., Heinen, T.J. a J., Kremer, M., Wunderlich, F.T.,

797 Jung, S., and Waisman, A. (2005). A Cre-inducible diphtheria toxin receptor mediates
798 cell lineage ablation after toxin administration. Nat. Methods *2*, 419–426.
799 34. Mendes, C.S., Bartos, I., Márka, Z., Akay, T., Márka, S., and Mann, R.S. (2015).
800 Quantification of gait parameters in freely walking rodents. BMC Biol. *13*, 1–11.
801 35. Gruner, J.A., and Altman, J. (1980). Swimming in the rat: Analysis of locomotor
802 performance in comparison to stepping. Exp. Brain Res. *40*, 374–382.
803 36. Pocratsky, A.M., Shepard, C.T., Morehouse, J.R., Burke, D.A., Riegler, A.S., Hardin,
804 J.T., Beare, J.E., Hainline, C., States, G.J., Brown, B.L., et al. (2020). Long ascending
805 propriospinal neurons provide flexible, context-specific control of interlimb
806 coordination. Elife *9*, 1–24.
807 37. Akay, T., and Murray, A.J. (2021). Relative Contribution of Proprioceptive and
808 Vestibular Sensory Systems to Locomotion: Opportunities for Discovery in the Age of
809 Molecular Science. Int. J. Mol. Sci. *22*, 1–18.
810 38. Horio, N., Yoshida, R., Yasumatsu, K., Yanagawa, Y., Ishimaru, Y., Matsunami, H.,
811 and Ninomiya, Y. (2011). Sour Taste Responses in Mice Lacking PKD Channels.
812 PLoS One *6*, e20007.
813 39. Pazour, G.J., Dickert, B.L., Vucica, Y., Seeley, E.S., Rosenbaum, J.L., Witman, G.B.,
814 and Cole, D.G. (2000). Chlamydomonas IFT 88 and Its Mouse Homologue, Polycystic
815 Kidney Disease Gene Tg 737, Are Required for Assembly of Cilia and Flagella. J. Cell
816 Biol. *151*, 709–718.
817 40. Haycraft, C.J., Zhang, Q., Song, B., Jackson, W.S., Detloff, P.J., Serra, R., and Yoder,
818 B.K. (2007). Intraflagellar transport is essential for endochondral bone formation.
819 Development *134*, 307–316.
820 41. Orts-Del'Immagine, A., Cantaut-Belarif, Y., Thouvenin, O., Roussel, J., Baskaran, A.,
821 Langui, D., Koëth, F., Bivas, P., Lejeune, F.-X.X., Bardet, P.-L.L., et al. (2020).

Sensory Neurons Contacting the Cerebrospinal Fluid Require the Reissner Fiber to Detect Spinal Curvature In Vivo. Curr. Biol. *30*, 827-839.e4.

42. Grillner, S., and El Manira, A. (2020). Current principles of motor control, with special reference to vertebrate locomotion. Physiol. Rev. *100*, 271–320.

43. Rudomin, P., and Schmidt, R.F. (1999). Presynaptic inhibition in the vertebrate spinal cord revisited. Exp. Brain Res. *129*, 1–37.

44. Wu, M.-Y., Carbo-Tano, M., Mirat, O., Lejeune, F.-X., Roussel, J., Quan, F.B., Fidelin, K., and Wyart, C. (2021). Spinal sensory neurons project onto the hindbrain to stabilize posture and enhance locomotor speed. Curr. Biol. *31*, 3315-3329.e5.

45. Skarlatou, S., Hérent, C., Toscano, E., Mendes, C.S., Bouvier, J., and Zampieri, N. (2020). Afadin Signaling at the Spinal Neuroepithelium Regulates Central Canal Formation and Gait Selection. Cell Rep. *31*, 107741.

46. Mathis, A., Mamidanna, P., Cury, K.M., Abe, T., Murthy, V.N., Mathis, M.W., and Bethge, M. (2018). DeepLabCut: markerless pose estimation of user-defined body parts with deep learning. Nat. Neurosci. *21*, 1281–1289.

47. Dewitz, C., Pimpinella, S., Hackel, P., Akalin, A., Jessell, T.M., and Zampieri, N. (2018). Nuclear Organization in the Spinal Cord Depends on Motor Neuron Lamination Orchestrated by Catenin and Afadin Function. Cell Rep. *22*, 1681–1694.

48. Susaki, E.A., Tainaka, K., Perrin, D., Yukinaga, H., Kuno, A., and Ueda, H.R. (2015). Advanced CUBIC protocols for whole-brain and whole-body clearing and imaging. Nat. Protoc. *10*, 1709–1727.

49. Madisen, L., Zwingman, T.A., Sunkin, S.M., Oh, S.W., Zariwala, H.A., Gu, H., Ng, L.L., Palmiter, R.D., Hawrylycz, M.J., Jones, A.R., et al. (2010). A robust and high-throughput Cre Repooting and characterization. Nat Neurosci *13*, 133–140.

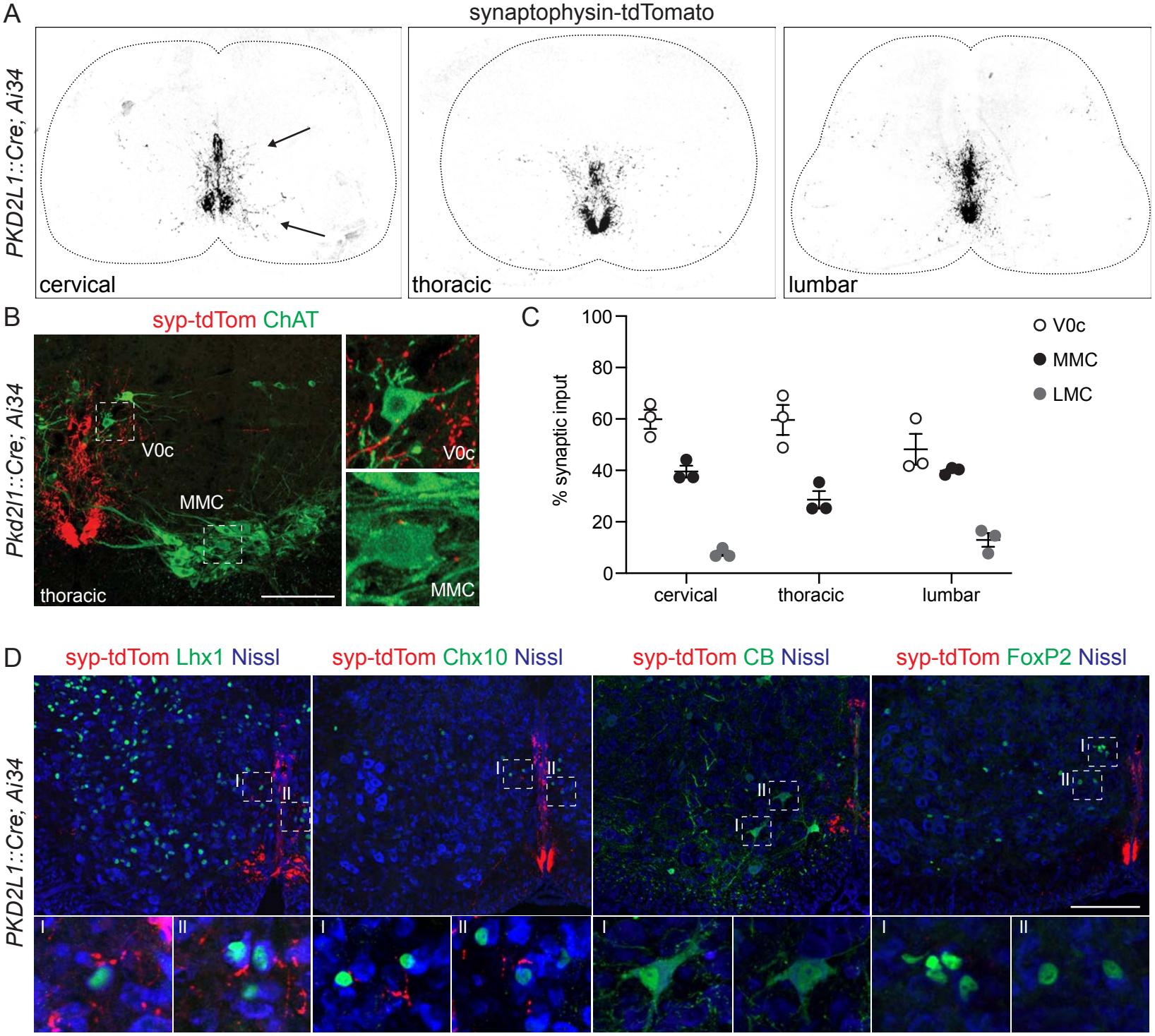
A
synaptophysin-tdTomato
PKD2L1::Cre; Ai34
cervical
thoracic
lumbar
B
syp-tdTom ChAT
Pkd2l1::Cre; Ai34
V0c
MMC
thoracic
V0c
MMC
C
% synaptic input
100
80
60
40
20
0
V0c
MMC
LMC
cervical
thoracic
lumbar
D
syp-tdTom Lhx1 Nissl
syp-tdTom Chx10 Nissl
syp-tdTom CB Nissl
syp-tdTom FoxP2 Nissl
PKD2L1::Cre; Ai34
I
II

Figure 1

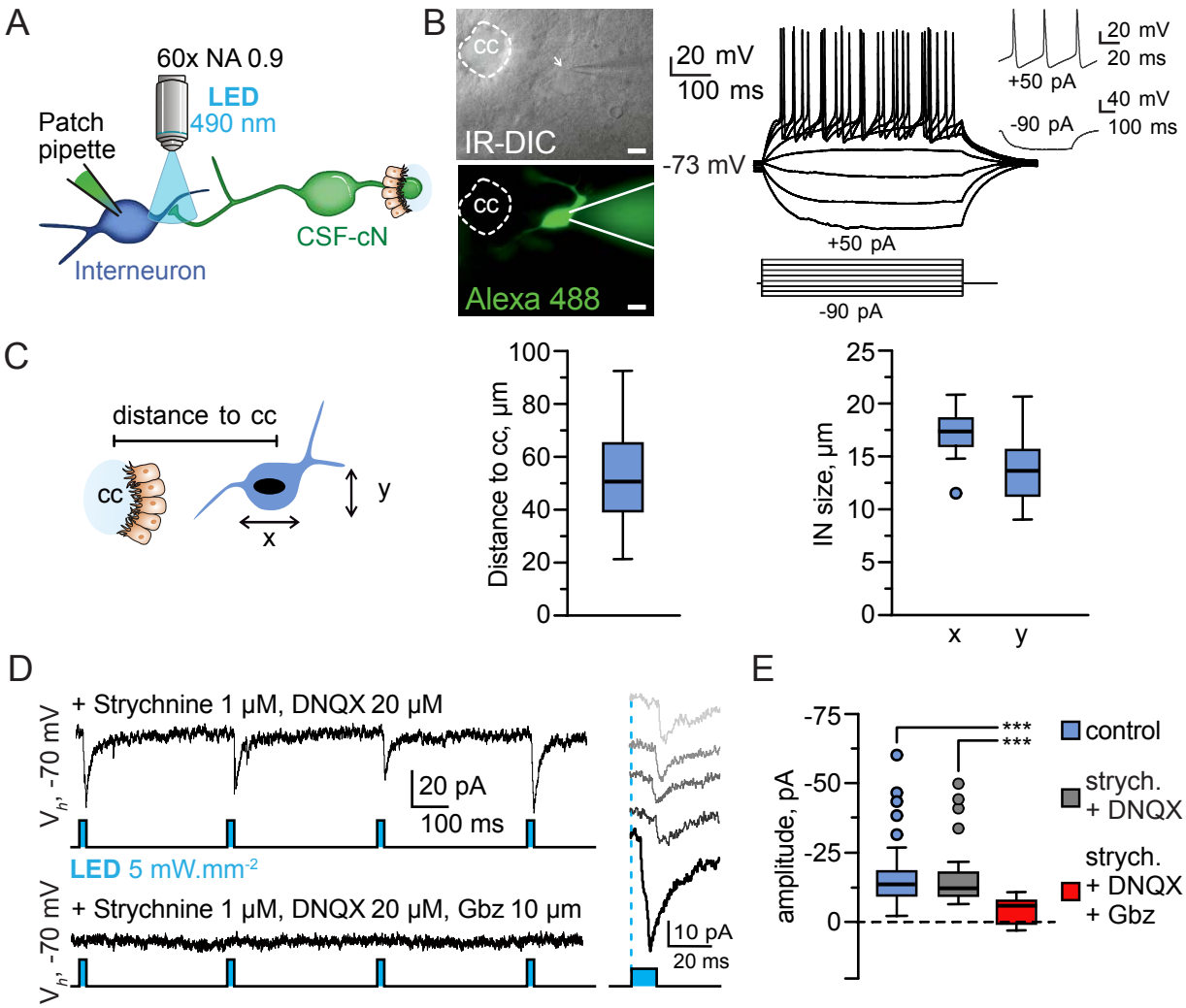
A
60x NA 0.9
LED
490 nm
Patch
pipette
CSF-cN
Interneuron
B
cc
IR-DIC
cc
Alexa 488
20 mV
100 ms
-73 mV
+50 pA
-90 pA
20 mV
20 ms
+50 pA
40 mV
100 ms
-90 pA
C
distance to cc
cc
x
y
Distance to cc, µm
100
80
60
40
20
0
IN size, µm
25
20
15
10
5
0
x
y
D
+ Strychnine 1 µM, DNQX 20 µM
V_h, -70 mV
20 pA
100 ms
LED 5 mW.mm-2
+ Strychnine 1 µM, DNQX 20 µM, Gbz 10 µm
V_h, -70 mV
10 pA
20 ms
E
amplitude, pA
-75
-50
-25
0
***
***
control
strych.
+ DNQX
strych.
+ DNQX
+ Gbz

Figure 2

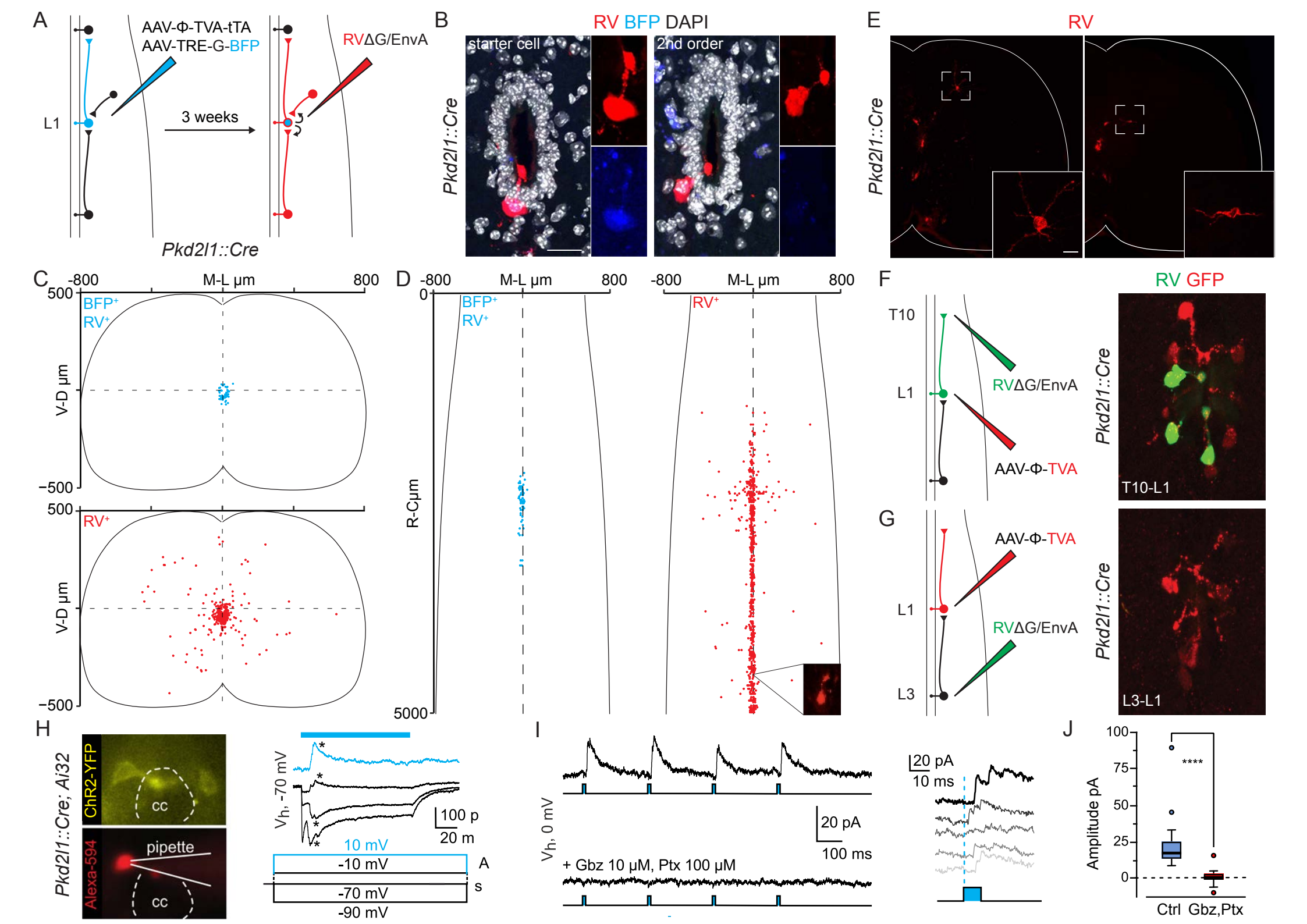
A
AAV-Φ-TVA-tTA
AAV-TRE-G-BFP
RVΔG/EnvA
L1
3 weeks
Pkd2l1::Cre
B
RV BFP DAPI
starter cell
2nd order
Pkd2l1::Cre
E
RV
Pkd2l1::Cre
C
-800
M-L µm
800
500
BFP+
RV+
V-D µm
−500
RV+
D
0
R-Cµm
5000
F
T10
L1
RVΔG/EnvA
AAV-Φ-TVA
RV GFP
Pkd2l1::Cre
T10-L1
G
L3
L3-L1
H
Pkd2l1::Cre; Ai32
ChR2-YFP
cc
Alexa-594
pipette
Vh, -70 mV
100 p
20 m
10 mV
-10 mV
-70 mV
-90 mV
A
s
I
Vh, 0 mV
20 pA
100 ms
+ Gbz 10 µM, Ptx 100 µM
20 pA
10 ms
J
Amplitude pA
100
75
50
25
0
****
Ctrl
Gbz,Ptx

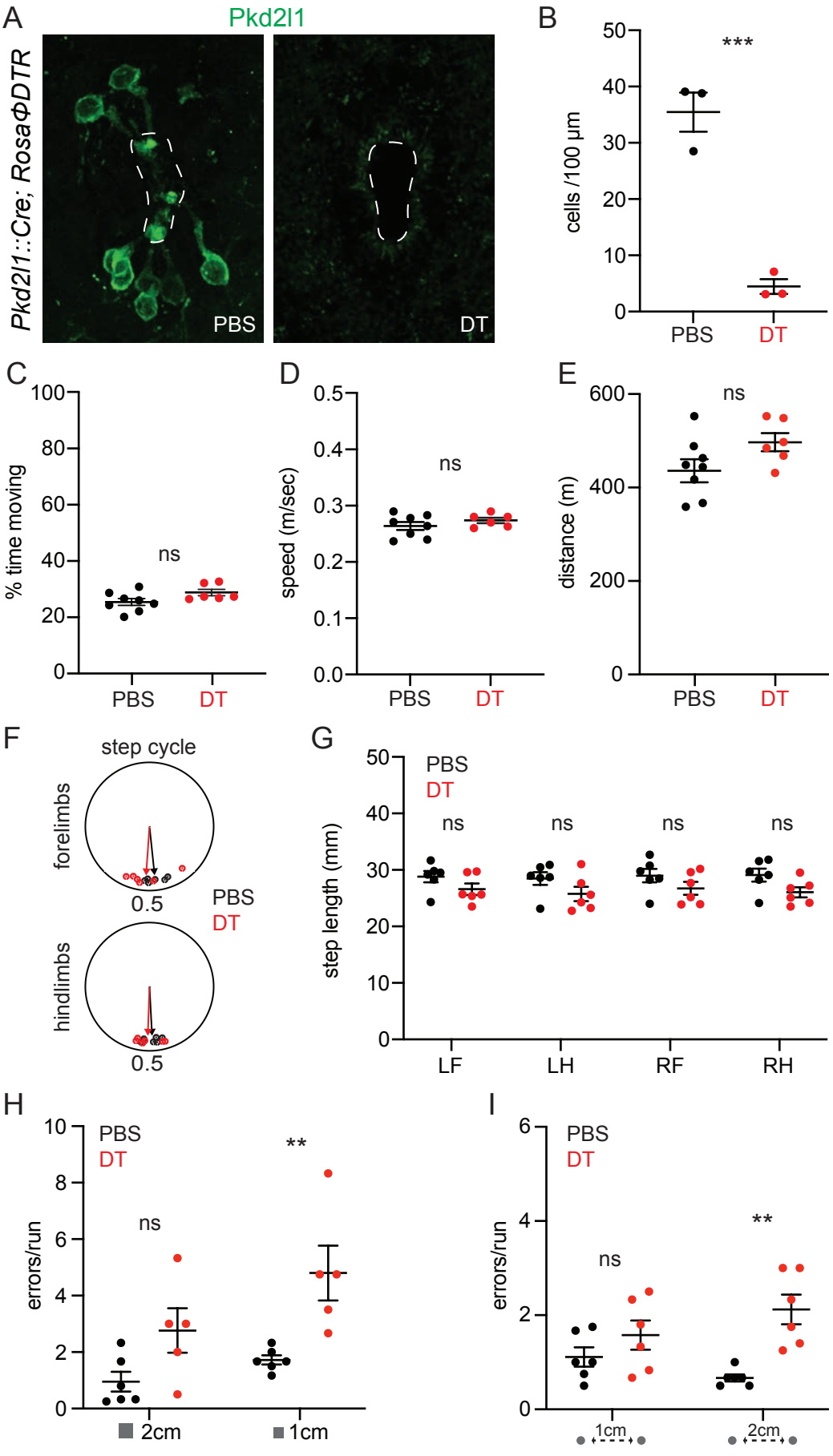
A
Pkd2l1
Pkd2l1::Cre; RosaΦDTR
PBS
DT
B
cells /100 µm
***
PBS
DT
C
% time moving
ns
D
speed (m/sec)
ns
E
distance (m)
ns
F
step cycle
forelimbs
hindlimbs
0.5
PBS
DT
G
step length (mm)
PBS
DT
ns
LF
LH
RF
RH
H
errors/run
PBS
DT
ns
**
2cm
1cm
I
errors/run
PBS
DT
ns
**
1cm
2cm

Figure 4

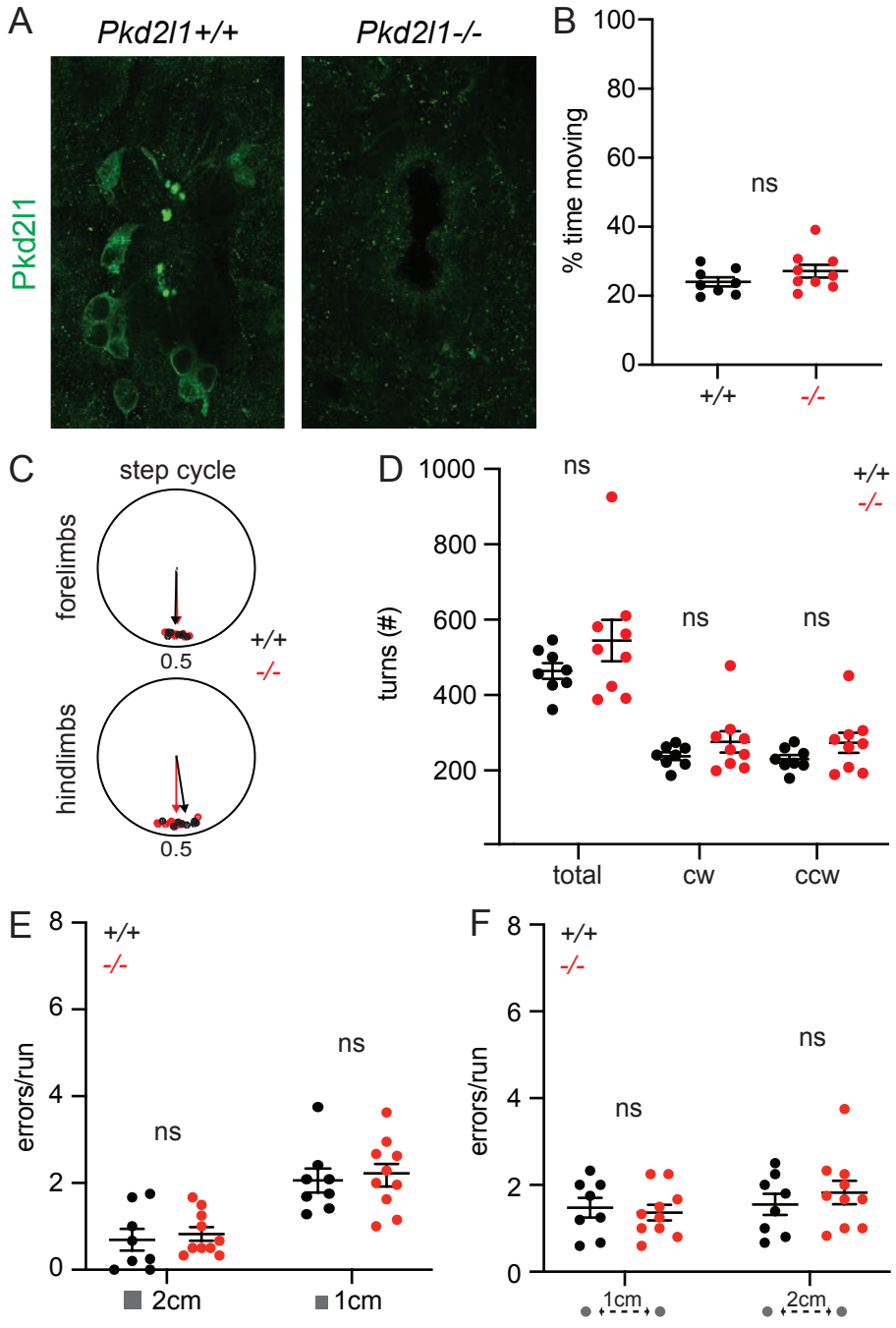
A
Pkd2l1+/+
Pkd2l1-/-
Pkd2l1
B
% time moving
ns
+/+
-/-
C
step cycle
forelimbs
hindlimbs
0.5
+/+
-/-
D
turns (#)
ns
total
cw
ccw
E
errors/run
2cm
1cm
F
errors/run
1cm
2cm

Figure 5

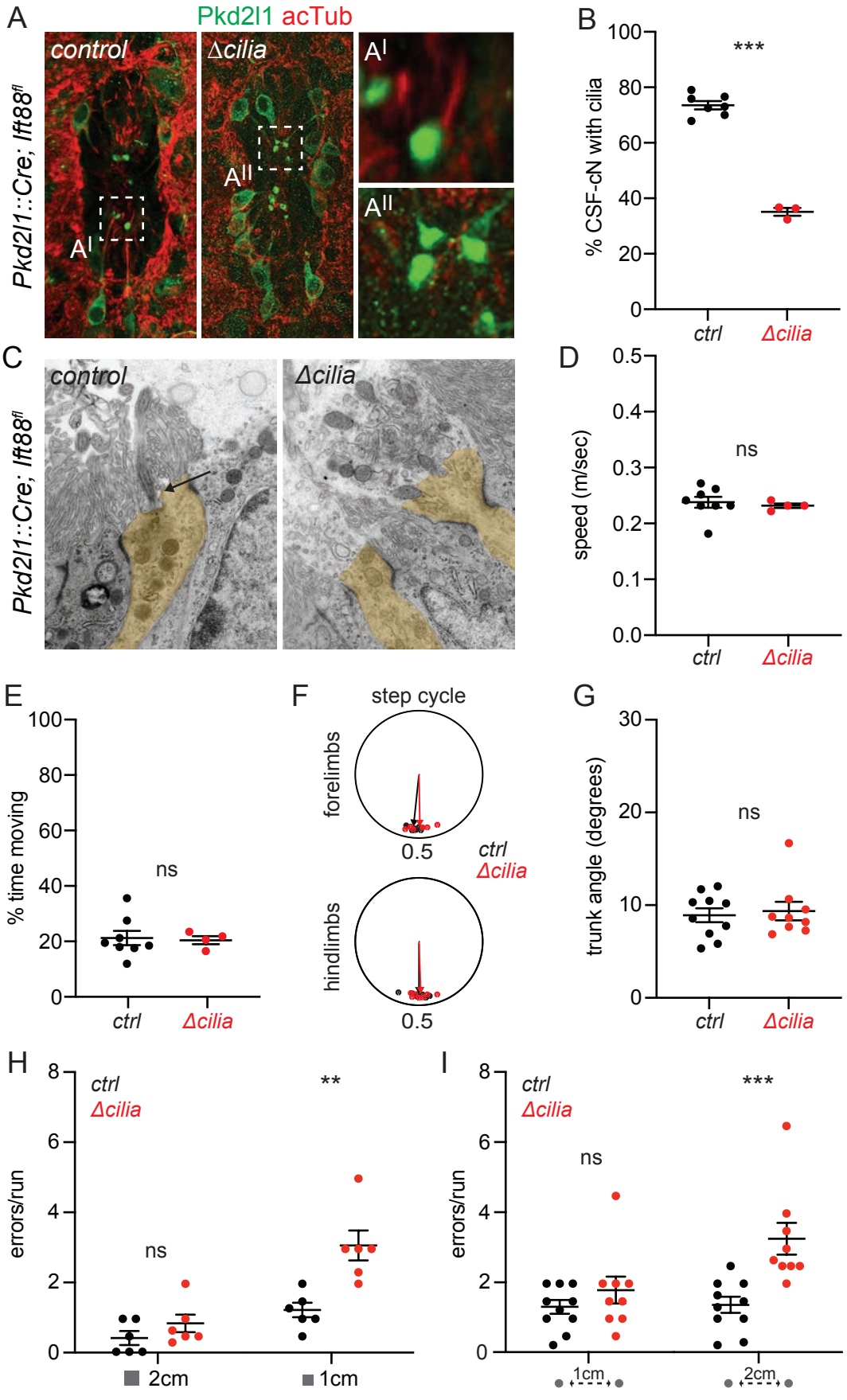
A
Pkd2l1 acTub
Pkd2l1::Cre; Ift88fl
control
Δcilia
AI
AII
B
% CSF-cN with cilia
***
ctrl
Δcilia
C
control
Δcilia
D
speed (m/sec)
ns
E
% time moving
ns
F
step cycle
forelimbs
hindlimbs
0.5
ctrl
Δcilia
G
trunk angle (degrees)
ns
H
errors/run
ctrl
Δcilia
**
ns
2cm
1cm
I
***
ns
1cm
2cm

Figure 6

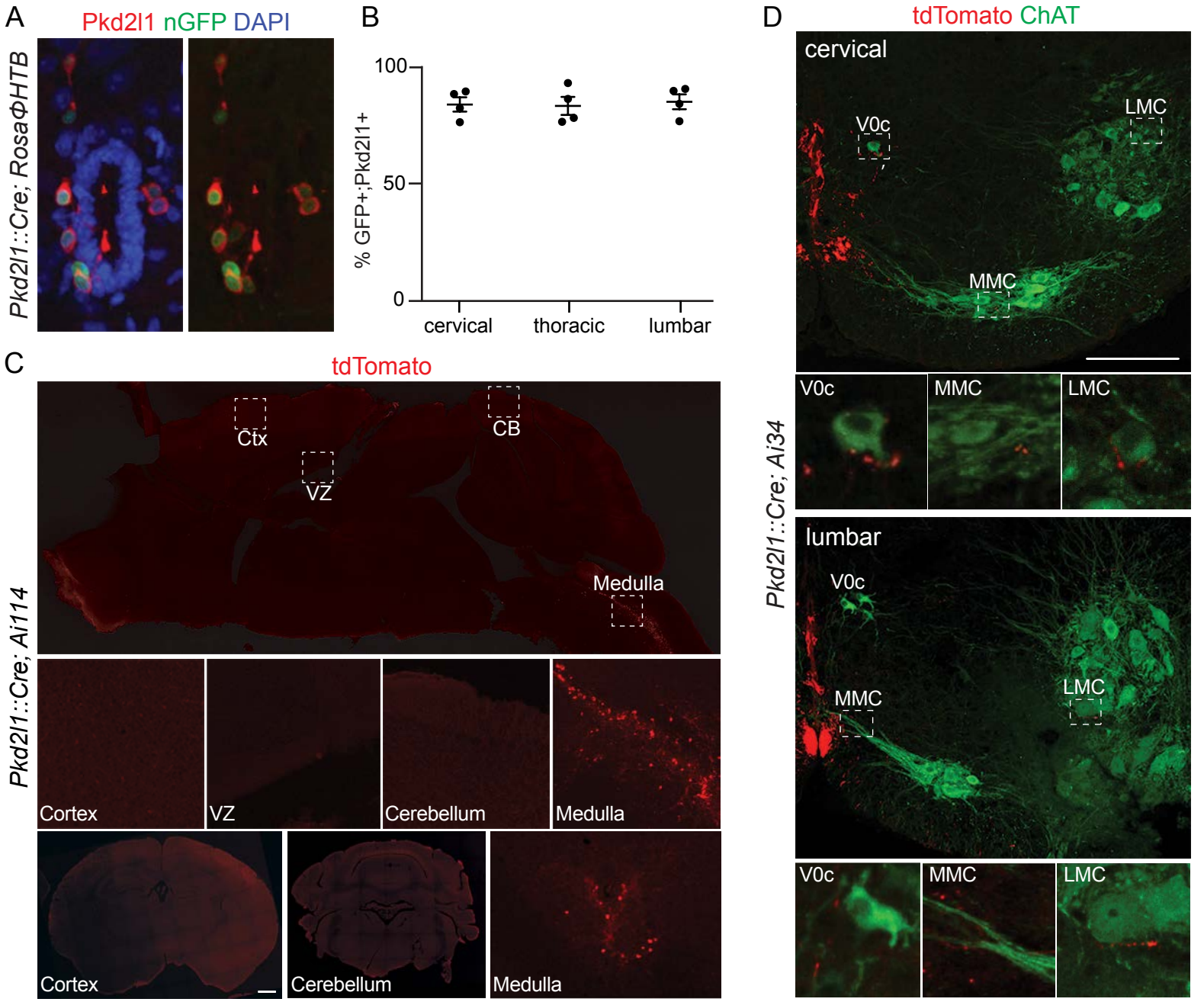
A
Pkd2l1 nGFP DAPI
Pkd2l1::Cre; RosaΦHTB
B
100
50
0
% GFP+;Pkd2l1+
cervical
thoracic
lumbar
C
tdTomato
Ctx
CB
VZ
Medulla
Pkd2l1::Cre; Ai114
Cortex
VZ
Cerebellum
Medulla
Cortex
Cerebellum
Medulla
D
tdTomato ChAT
cervical
V0c
LMC
MMC
V0c
MMC
LMC
lumbar
V0c
MMC
LMC
Pkd2l1::Cre; Ai34
V0c
MMC
LMC

Figure S1

Figure S1. Specificity of CSF-cN genetic targeting. Related to Figure 1.

A) Representative image of Pkd2l1^{+}; nuclear GFP^{+} neurons around the central canal of *Pkd2l1::Cre; RosaΦHTB* mice.

B) Quantification of Pkd2l1^{+}; nuclear GFP^{+} neurons at cervical, thoracic, and lumbar spinal segments (cervical 182/220 cells, thoracic 198/230 cells, lumbar 179/209 cells, n=4; Mean±SEM).

C) Tomato expression in the brain of P7 *Pkd2l1::Cre; RosaΦtdTomato* mice (cortex, Ctx; ventricular zone, VZ; cerebellum, CB). Scale bar: 1mm.

D) Representative pictures of synaptophysin-tdTomato synapses on ChAT^{+} V0c, MMC, and LMC neurons at cervical and lumbar segments of P7 *Pkd2l1::Cre; RosaΦsynaptophysin-tdTomato* mice (Magnifications show single z-planes).

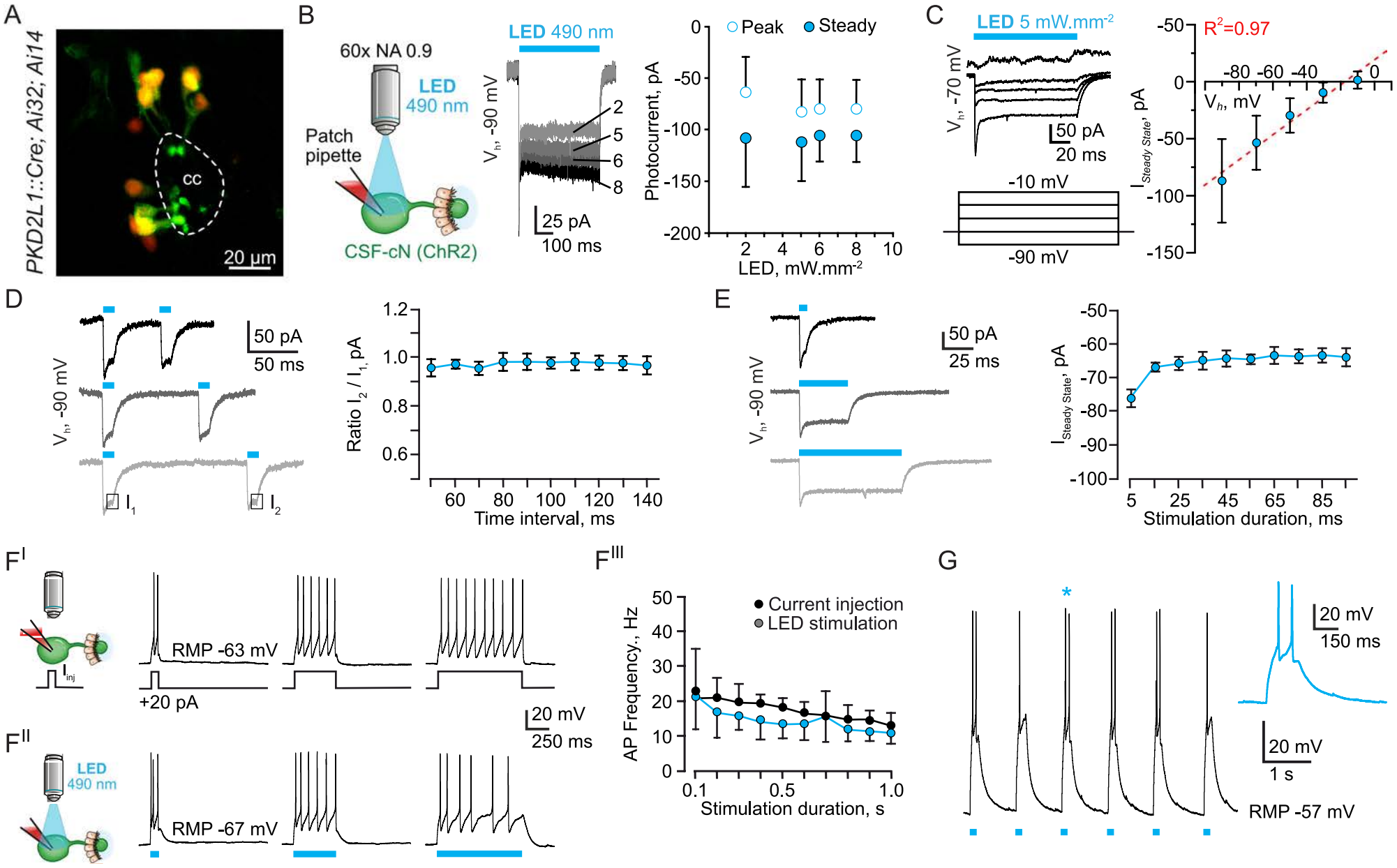
A
PKD2L1::Cre; Ai32; Ai14
cc
20 µm
B
60x NA 0.9
LED
490 nm
Patch
pipette
CSF-cN (ChR2)
LED 490 nm
Vh, -90 mV
2
5
6
8
25 pA
100 ms
Peak
Steady
Photocurrent, pA
LED, mW.mm-2
C
LED 5 mW.mm-2
Vh, -70 mV
50 pA
20 ms
-10 mV
-90 mV
R2=0.97
ISteady State, pA
Vh, mV
D
Vh, -90 mV
50 pA
50 ms
I1
I2
Ratio I2 / I1, pA
Time interval, ms
E
Vh, -90 mV
50 pA
25 ms
ISteady State, pA
Stimulation duration, ms
FI
Iinj
RMP -63 mV
+20 pA
20 mV
250 ms
FII
LED
490 nm
RMP -67 mV
FIII
Current injection
LED stimulation
AP Frequency., Hz
Stimulation duration, s
G
20 mV
150 ms
20 mV
1 s
RMP -57 mV

Figure S2

Figure S2. Optogenetic activation of CSF-cN. Related to Figure 2.

A) Representative confocal image of an acute lumbar spinal cord slice (250 µm, cc: central canal) obtained from a *Pkd2l1::Cre; RosaΦChrR2*; *RosaΦtdTomato* mice showing selective ChR2 and tdTomato expression in CSF-cN around the central canal.

B) Cartoon of the protocol used to record and photoactivate CSF-cN with the representative traces recorded in VC mode (V_h of -90 mV) in one CSF-cN upon exposure to a 500 ms light pulse of increasing power (LED: 490 nm, 2 to 8 $mW.mm^{-2}$). Right, summary graph of the average photocurrent amplitude as a function of the LED power and measured at the initial peak (blue circles) and at the steady (open circles) currents (mean ± SD, n=12, 16, 13 and 14 for 2, 5, 6 and 8 $mW.mm^{-2}$, respectively).

C) Representative traces of photocurrents elicited with a 100 ms light-pulse and recorded in one CSF-cN at V_h of -70 mV as a function of the voltage (V_{Step}: -90 to -10 mV, 20 mV increments). Note that, at each test potential, the light pulse was applied 100 ms after the start of the step to reach stable baseline before ChR2 activation. Right, graph of the average current-voltage relationship (V_h of -70 mV, V_{Step}: -90 to -10 mV, 20 mV increments) of the ChR2-mediated photocurrent. The linear fit (red dashed line, R^2=0.97) of the data points indicate that the current reversal potential is observed around -10 mV (mean ± SD, n=67; see text for details).

D) Left, representative photocurrents recorded in one CSF-cN and elicited with two light pulses (10 ms duration) separated by a time interval of 50, 90 and 140 ms (Top to bottom traces, respectively). Right, graph of the average amplitude ratio (I_2/I_1) of the currents elicited by the 2nd pulse (I_2) divided by that upon exposure to the 1st pulse (I_1) and presented as a function of the time interval (50 to 120 ms, 10 ms increments, V_h -90 mV; mean ± SD, n=8).

E) Left, representative photocurrents recorded in one CSF-cN upon exposure to light pulses for 5, 45 and 95 ms (Top to bottom traces, respectively). Right, graph of the average amplitude for

the steady state photocurrents elicited with one light pulse of increasing duration (5 to 95 ms, 10 ms increments, V_h -90 mV; mean ± SD, n=11).

F) Representative traces of the action potential (AP) discharge recorded in one CSF-cN (CC mode, RMP: -63 mV) and triggered in the same neuron by either DC current injections (+20 pA, F^{I}) or upon exposure to a light pulse (LED, F^{II}) of increasing duration (100 ms with 100 ms increments; n=7). (F^{III}) Graph of the average AP frequency (Hz) triggered by either DC current injection (black circles) or exposure to light (blue circles) of increasing duration (100 ms to 1 s, 100 ms increments; mean ± SD, n=7).

G) Representative trace of AP discharge recorded in one CSF-cN (CC mode, RMP: -57 mV) and triggered by repetitive light pulses (10 ms every second). Inset shows enlarged trace from the illustrated recording (Left, *). Except for panel B, light pulse (blue bars) power was set at 5 $mW.mm^{-2}$.

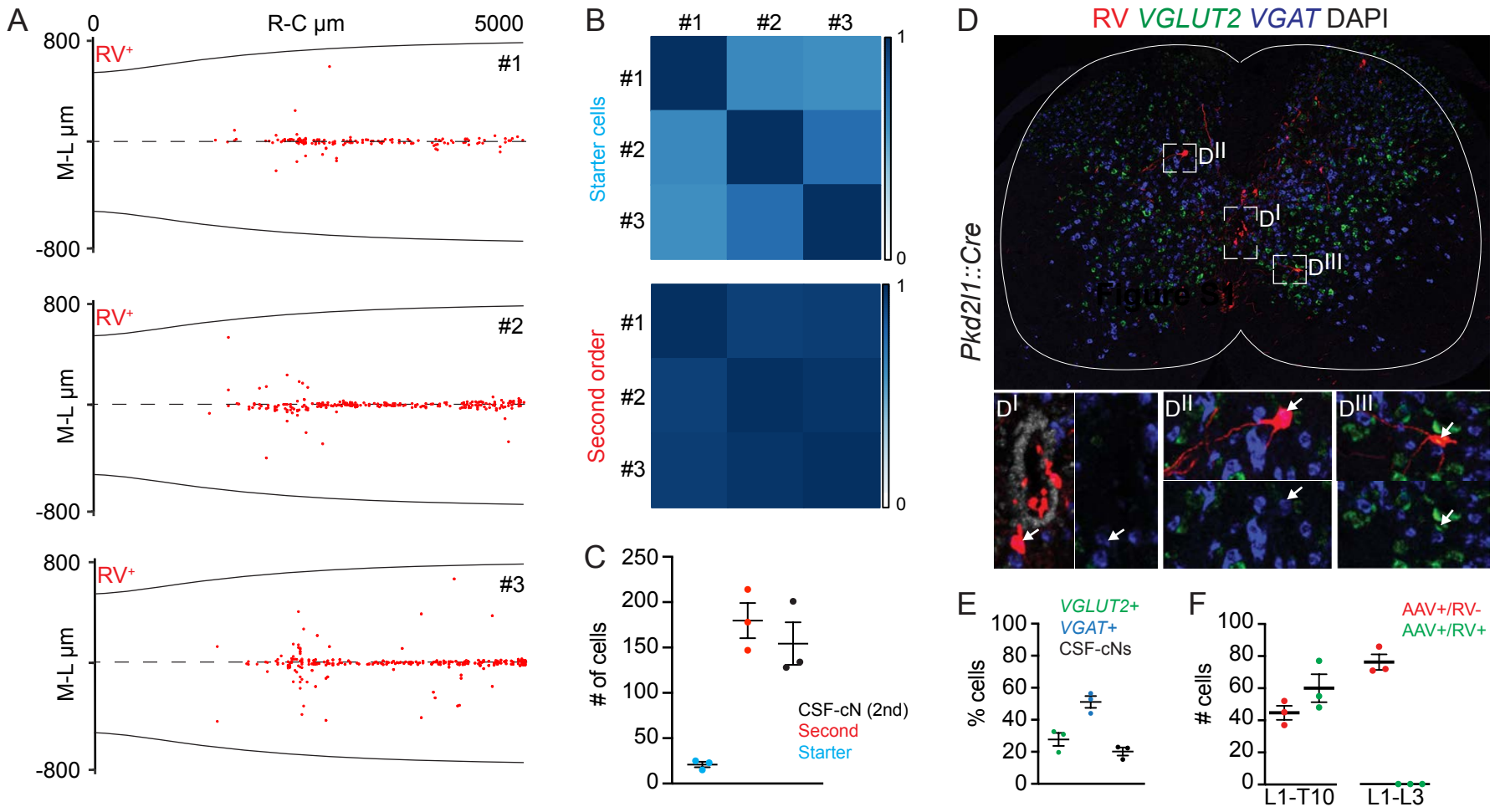
A
0
R-C µm
5000
800
RV+
#1
M-L µm
-800
800
RV+
#2
M-L µm
-800
800
RV+
#3
M-L µm
-800
B
#1
#2
#3
Starter cells
#1
#2
#3
1
0
Second order
#1
#2
#3
1
0
C
250
200
150
100
50
0
# of cells
CSF-cN (2nd)
Second
Starter
D
RV VGLUT2 VGAT DAPI
Pkd2l1::Cre
DII
DI
DIII
Tissue s
DI
DII
DIII
E
VGLUT2+
VGAT+
CSF-cNs
100
80
60
40
20
0
% cells
F
AAV+/RV-
AAV+/RV+
100
80
60
40
20
0
cells
L1-T10
L1-L3

Figure S3

Figure S3. Rabies monosynaptic tracing from CSF-cN. Related to Figure 3.

A) Digital reconstruction of RV^+ second order cells (red) rostro-caudal position. Each plot represents one animal.

B) Correlation analysis of starter cells (top) and second order cells (bottom) positional coordinates. The scale indicates correlation values.

C) Number of starter cells (blue), second order cells (red) and second order CSF-cN in individual rabies tracing experiments (black).

D) Multiplexed fluorescent in situ hybridization analysis of RV^+ neurons showing excitatory ($VGLUT2^+$) and inhibitory ($VGAT^+$) second order cells.

E) Proportion of $VGLUT2^+$ and $VGAT^+$ second order neurons (n=3).

F) Quantification of AAV^+/RV^- and AAV^+/RV^+ cells labelled after injection of AAV-FLEX-TVAmCherry at L1 and RVΔG-GFP/EnvA at either T10 or L3.

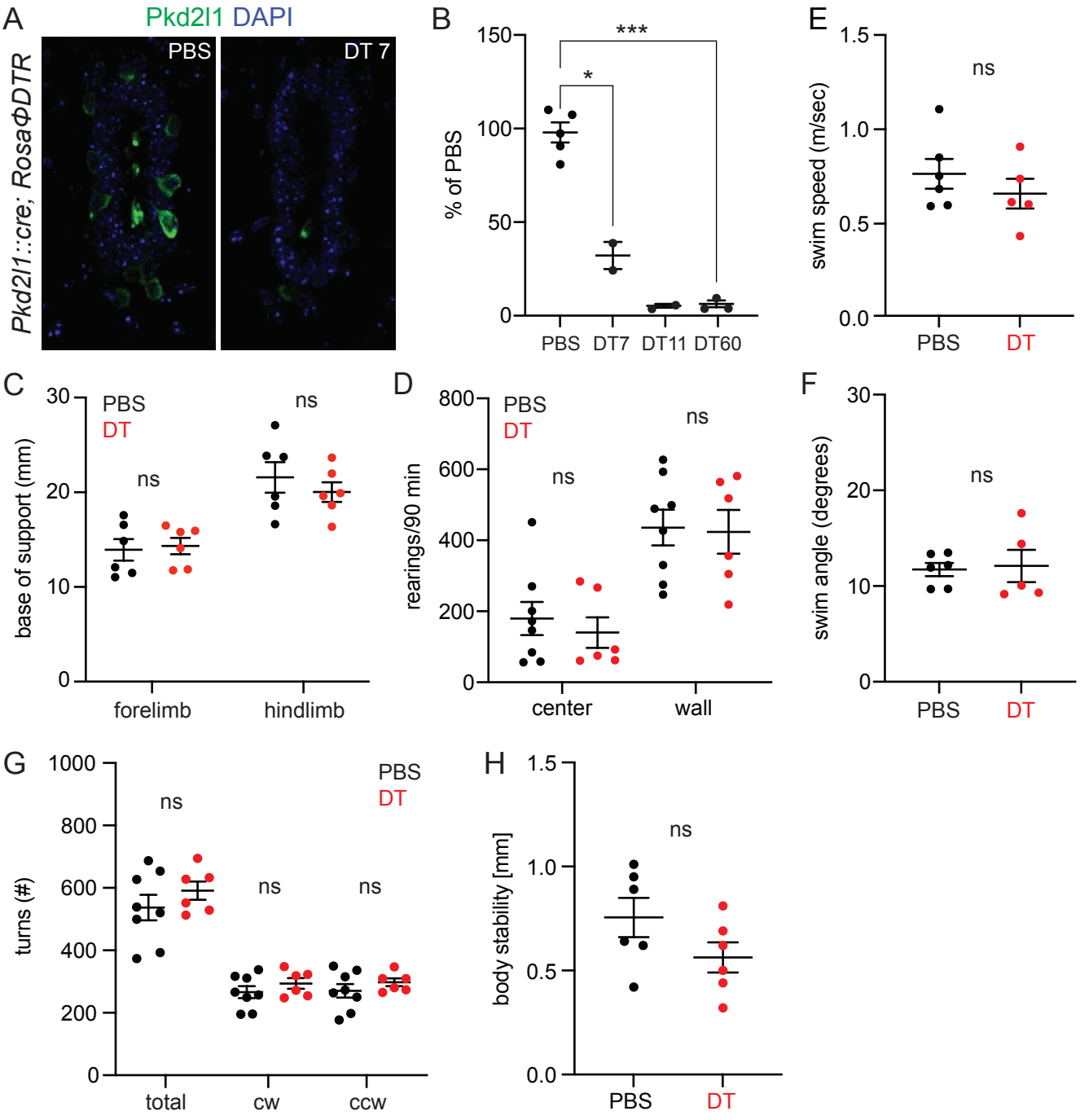
A
Pkd2l1 DAPI
Pkd2l1::cre; RosaΦDTR
PBS
DT 7
B
% of PBS
150
100
50
0
***
*
PBS
DT7
DT11
DT60
E
swim speed (m/sec)
1.5
1.0
0.5
0.0
ns
PBS
DT
C
base of support (mm)
30
20
10
0
PBS
DT
ns
ns
forelimb
hindlimb
D
rearings/90 min
800
600
400
200
0
PBS
DT
ns
ns
center
wall
F
swim angle (degrees)
30
20
10
0
ns
PBS
DT
G
turns (#)
1000
800
600
400
200
0
PBS
DT
ns
ns
ns
total
cw
ccw
H
body stability [mm]
1.5
1.0
0.5
0.0
ns
PBS
DT

Figure S4

Figure S4. Behavioral analysis of CSF-cN ablated mutant mice. Related to Figure 4.

A) Representative images of Pkd2l1 staining in adult *Pkd2l1::Cre; RosaΦDTR* mice 7 days after PBS (left) or DT-injection (right).

B) Percentage of Pkd2l1^{+} cells in respect to the PBS control at 7 days, 11 days and 60 days after DT treatment in adult *Pkd2l1::Cre; RosaΦDTR* mice.

C) Base of support of forelimbs (left) and hindlimbs (right) in Pkd2l1::Cre; RosaΦDTR mice 14 days after PBS (n=6) or DT (n=6) treatment.

D) Spontaneous rearing during a 90 min open field test in the center of the arena (left) or against the wall (right) in *Pkd2l1::Cre; RosaΦDTR* mice 14 days after PBS (n=8) or DT (n=6) treatment.

E) Speed during swimming task in *Pkd2l1::Cre; RosaΦDTR* mice 14 days after PBS (n=6) or DT (n=5) treatment.

F) Quantification of trunk angle between body axis and water line during swimming task in *Pkd2l1::Cre; RosaΦDTR* mice 14 days after PBS (n=6) or DT (n=5) treatment.

G) Analysis of turning behavior (total, clockwise, and counterclockwise turns) during a 90 min open field test in *Pkd2l1::Cre; RosaΦDTR* mice 14 days after PBS (n=8) or DT (n=6) treatment.

H) Body stability analysis during walking on a Plexiglas runway in *Pkd2l1::Cre; RosaΦDTR* mice 14 days after PBS (n=8) or DT (n=6) treatment.

Mean±SEM, paired t-test, ns $p>0.05$.

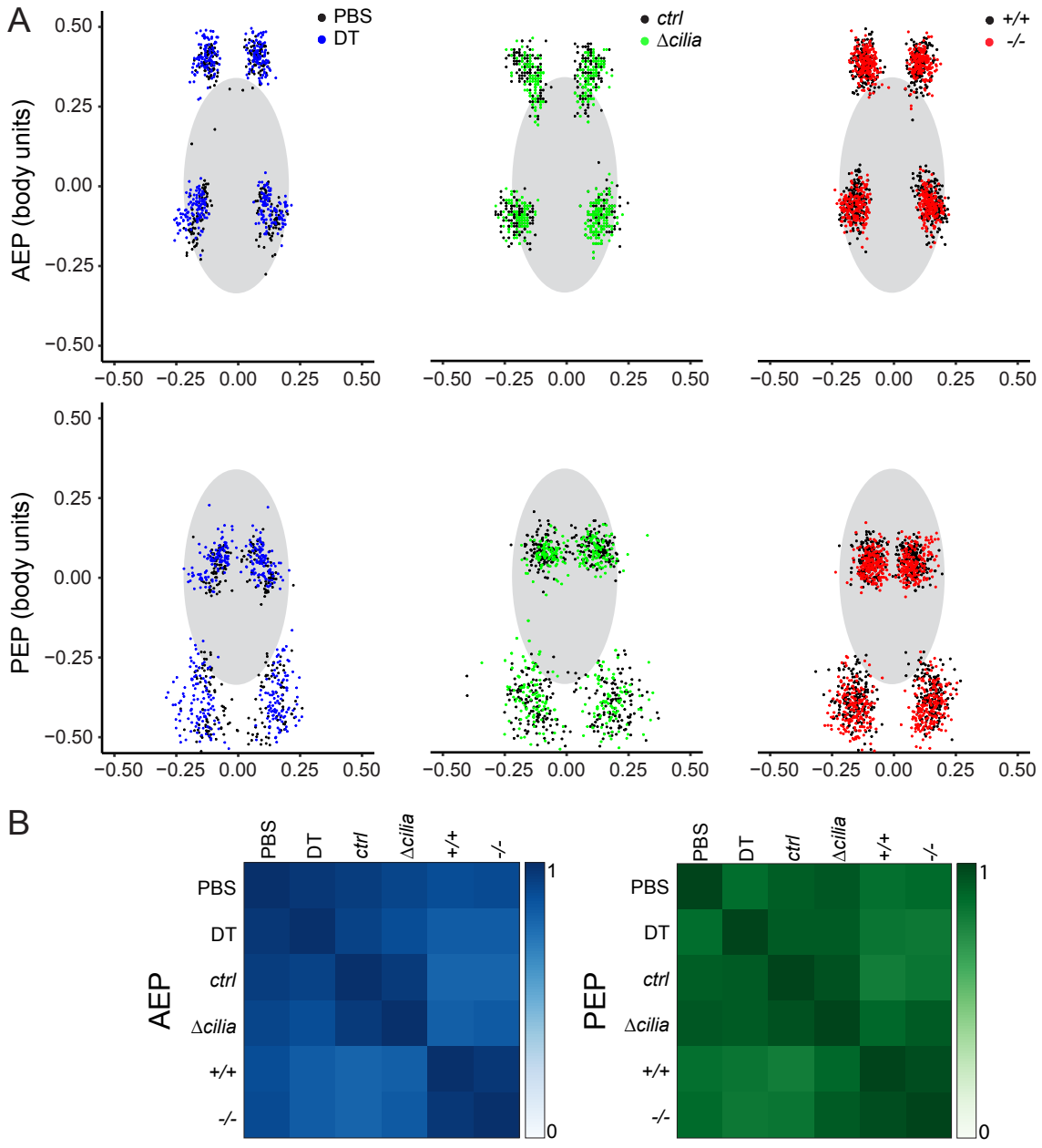
A
AEP (body units)
PEP (body units)
PBS
DT
ctrl
Δcilia
+/+
-/-
0.50
0.25
0.00
−0.25
−0.50
B
AEP
PEP
PBS
DT
ctrl
Δcilia
+/+
-/-
1
0

Figure S5

Figure S5. Footprint clustering analysis. Related to Figures 4, 5 and 6.

A) Footprint clustering during walking on a Plexiglas runway in CSF-cN ablated (left), *Δcilium* (center), and *Pkd2l1 -/-* (right) mice. AEP, anterior extreme position; PEP, posterior extreme position.

B) Correlation analysis of footprint positions for AEP (left) and PEP (right). The scale indicates correlation values.

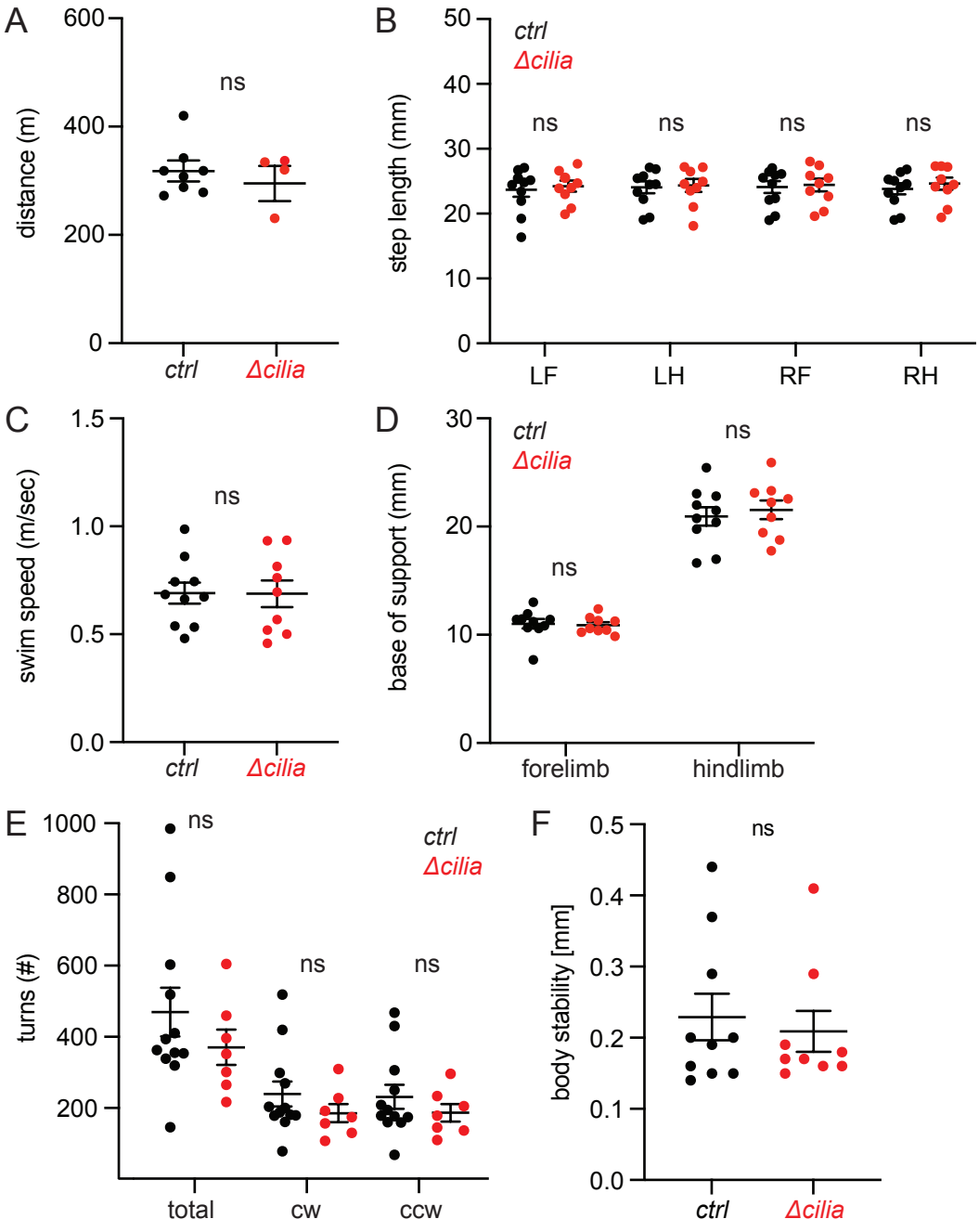
A
distance (m)
600
400
200
0
ns
ctrl
Δcilia
B
step length (mm)
50
40
30
20
10
0
ctrl
Δcilia
ns
ns
ns
ns
LF
LH
RF
RH
C
swim speed (m/sec)
1.5
1.0
0.5
0.0
ns
ctrl
Δcilia
D
base of support (mm)
30
20
10
0
ctrl
Δcilia
ns
ns
forelimb
hindlimb
E
turns (#)
1000
800
600
400
200
ns
ctrl
Δcilia
ns
ns
total
cw
ccw
F
body stability [mm]
0.5
0.4
0.3
0.2
0.1
0.0
ns
ctrl
Δcilia

Figure S6

Figure S6. Elimination of cilia from CSF-cN does not affect locomotor activity and gait parameters. Related to Figure 6.

A) distance traveled during a 90 min open field test in adult control (n=8) and Δ*cilia* (n=4) mice.

B) Step length in adult control (n=10) and Δ*cilia* (n=9) mice (LF left forelimb, LH left hindlimb, RF right forelimb, RH right hindlimb).

C) Speed during swimming task in adult control (n=10) and Δ*cilia* (n=9) mice.

D) Base of support of forelimbs (left) and hindlimbs (right) in adult control (n=10) and Δ*cilia* (n=9) mice.

E) Analysis of turning behavior (total, clockwise, and counterclockwise turns) during a 90 min open field test in adult control (n=12) and Δ*cilia* (n=7) mice.

F) Body stability analysis during walking on a Plexiglas runway in adult control (n=10) and Δ*cilia* (n=9) mice.

Mean±SEM, paired t-test, ns $p>0.05$.